LBNL-41096
UC-405
Preprint

ERNEST ORLANDO LAWRENCE
BERKELEY NATIONAL LABORATORY

On the Structure and Dynamics of Tornado-Like Vortices

David S. Nolan and Brian F. Farrell

Computing Sciences Directorate

November 1997

Submitted to
Journal of the
Atmospheric Sciences

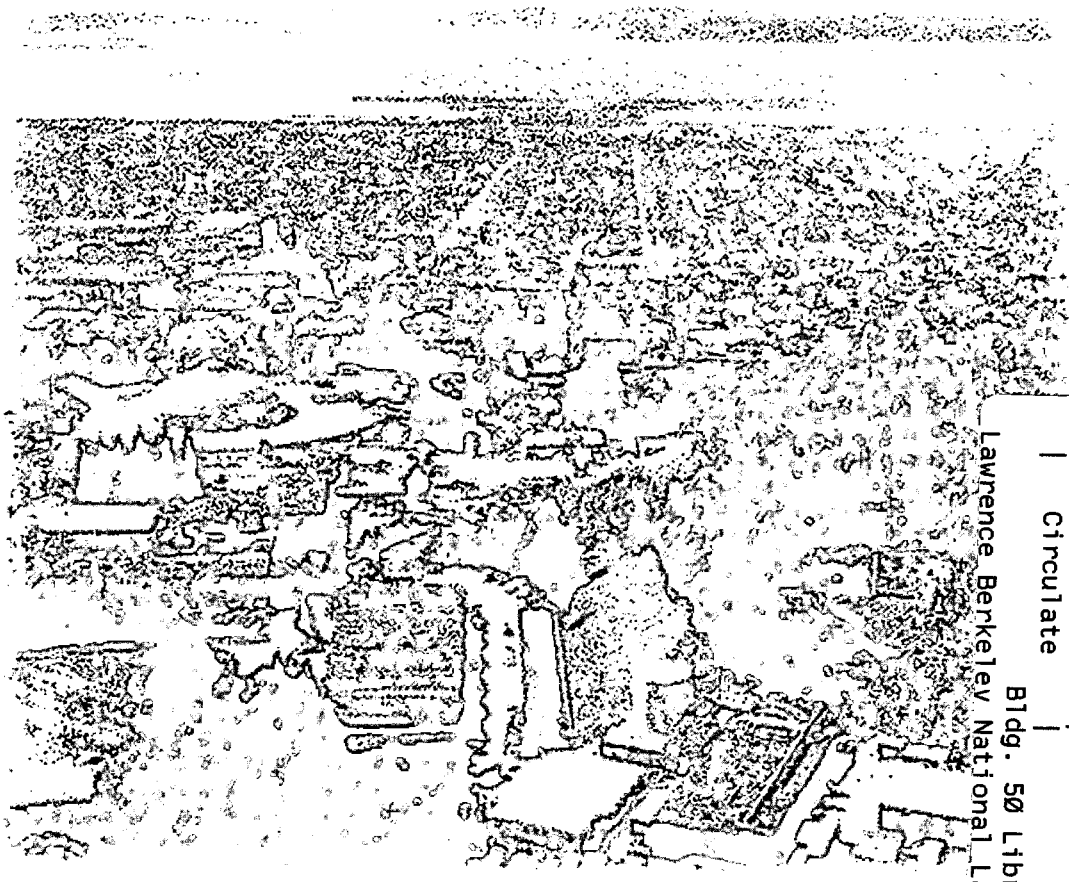

DISCLAIMER

LBNL-41096

ON THE STRUCTURE AND DYNAMICS OF TORNADO-LIKE VORTICES

David S. Nolan*
Mathematics Department
Computing Sciences Directorate
Lawrence Berkeley National Laboratory
Berkeley, CA 94720

Brian F. Farrell
Department for Earth and Planetary Sciences
Harvard University
Cambridge, MA 02138

Submitted to *Journal of the Atmospheric Sciences*

November 1997

*Corresponding author address: 50A-2152, Lawrence Berkeley National Laboratory, 1 Cyclotron Road, Berkeley, CA 94720; *nolan@math.lbl.gov*. This author's work was supported in part by the Applied Mathematical Sciences Subprogram of the Office of Energy Research, U.S. Department of Energy, under Contract DE-AC03-76SF00098.

Abstract

The structure and dynamics of axisymmetric tornado-like vortices are explored with a numerical model of axisymmetric incompressible flow based on recently developed numerical techniques. The model is first shown to compare favorably with previous results, and is then used to study the effects of varying the major parameters controlling the vortex: the strength of the convective forcing, the strength of the rotational forcing, and the magnitude of the model eddy viscosity. The results of simulations with each of these parameters varying independently suggest that while maximum windspeeds are proportional to the strength of the convective forcing, the structure and time-dependent behavior of the vortex depend almost exclusively on the ratio of the rotational forcing to the model eddy viscosity parameter.

For certain values of the swirl ratio, which is a measure of the ratio of the azimuthal velocities to the radial velocities of the fluid entering the vortex core, the flow in the vortex core may be either steady or oscillating. These oscillations, when present, are caused by axisymmetric disturbances propagating down towards the surface from above. Attempts to identify these disturbances with linear waves associated with the shears of the mean azimuthal and vertical wind give mixed results.

The parameter space defined by the choices for the rotation rate and the eddy viscosity is further explored with a large set of numerical simulations. For much of this parameter space we find that the vortex structure and time-dependent behavior dependence on the ratio of the rotational forcing to the eddy viscosity is confirmed. We also find that for higher Reynolds numbers, the maximum possible windspeed increases, and the rotational forcing necessary to achieve that windspeed decreases. Physical reasoning is used to explain this behavior, and implications for tornado dynamics are discussed.

1 Introduction

The use of numerical models has been one of the leading contributors to advances in our understanding of the causes and dynamics of the tornado phenomenon. This method of study can generally be divided into two categories: thunderstorm-scale simulations and tornado-scale simulations. In the former category, pioneered by Klemp and Wilhemson (1978), three-dimensional cloud models are used to numerically simulate the formation and dynamics of the thunderstorms that are responsible for tornado formation. While the low resolution of these earlier models could only hope to simulate the thunderstorm-scale environment that is believed to lead to tornado formation, Wicker and Wilhelmson (1995) recently reported the simulation of tornado-like features within a modelled thunderstorm. Tornado-scale models, pioneered by Rotunno (1977), assume a particular environment of rotation coupled with convection to create an intense vortex near the surface. These models are intended to provide the details of the wind field in the tornado and an understanding of the dynamics that lead to that flow structure. Until recently, most tornado-scale numerical models assumed the tornado to be axisymmetric, thereby reducing the problem from three dimensions to two dimensions in cylindrical coordinates.

Laboratory models, pioneered by Ward (1972), were the first to provide direct measurements of the wind field associated with "tornado-like" vortices - a term which could apply to any vortex caused by the convergence of rotating fluid along a lower boundary. (These would also include waterspouts and dust-devils, for example). For this reason, it seems, the early numerical

modellers simulated the environment of the laboratory apparatus rather than that of a thunderstorm. That is, the vortex was driven by forcing rotating flow into the sides of the domain and drawing fluid out the top with some kind of outflow boundary conditions.

A significant result is that numerical models have been able to reproduce many of the features observed in laboratory vortices. The most universal feature of the laboratory results is the way in which the flow through the vortex depends on a nondimensional parameter known as the swirl ratio:

$$S = \frac{\Gamma r_0}{2Qh} \tag{1.1}$$

where Γ is the circulation of the air as it enters the convection region in the apparatus, r_0 is the radius of the updraft, Q is the volume flow rate per unit axial length, and h is the depth of the inflow region (Church et al. 1979). As the value of the swirl parameter is increased, the vortex goes through various stages, as depicted in Figure 1: for S<0.1, there is no concentrated vortex at the surface. For larger values, a concentrated vortex does appear at the surface, and at some height above it there is a "vortex breakdown" where the flow transitions from a tight, laminar vortex to a broader, turbulent state. The vortex breakdown [Harvey (1962); Benjamin (1962); Lugt (1989)] is considered to be an axisymmetric analogue to the hydraulic jump phenomenon observed in channel flows. As S is increased, the altitude of the vortex breakdown decreases, until around S=0.45 the breakdown is just above the surface. This state has been referred to as a "drowned vortex jump," and is generally associated with having the highest near-surface azimuthal wind velocities. When S is further increased, the vortex breakdown reaches the surface and the vortex changes to a "two-celled" structure, where there is a downward recirculation in the vortex core and the radius of maximum winds substantially increases. Still larger values of S results in the appearance of

multiple vortices rotating around the vortex core. Three-dimensional models have also reproduced this multiple vortex phenomenon [Rotunno (1984); Lewellen (1993)]. A general review of the results of laboratory modelling of tornado-like vortices can be found in Church and Snow (1993).

Wilson and Rotunno (1986), used a model based on earlier work by Rotunno (1979,1984) to address the validity of various approximate laminar solutions for swirling boundary layers. They found good agreement with those solutions and with laboratory results. Howells, et al. (1988) focused instead on the dynamics over a wide range of swirl ratios and eddy viscosities, and studied the effect of no-slip versus free-slip lower boundary conditions. Their results demonstrated that the combination of high swirl ratio, low eddy viscosity, and the no-slip boundary conditions produced the highest near-surface windspeeds. This combination (low viscosity but no-slip boundary conditions) may be counter-intuitive at first, but Howells et al. (1988) demonstrated was the importance of a thin but strong inward jet at the surface which in the no-slip case drives the fluid above the jet much closer to r=0 than is possible with free-slip conditions.

The most recent efforts to study tornadic vortices with an axisymmetric model have been by Fiedler (1993,1994,1995) whose motivation was to determine the maximum velocities a surface vortex could achieve as compared to the velocity associated with the "thermodynamic speed limit" [Lilly (1969); Fiedler and Rotunno (1986)]. This estimated speed limit is made by matching the minimum surface pressure, calculated from hydrostatic integration of the overhead thermodynamic profile, with the central pressure deficit of a Rankine vortex or some other vortex profile. For a Rankine vortex, which has solid body rotation $v = v_{max} r / r_{max}$ out to some radius r_{max}, and a potential flow $v = v_{max} r_{max} / r$ outside of r=r_{max}, the pressure deficit Δp_{cyc} at r=0 due to cyclostrophic balance must be:

$$\Delta p_{cyc} = -\int_0^\infty \rho \frac{v^2}{r} dr = -\int_0^{r_{max}} \rho \frac{v_{max}^2}{r_{max}^2} r dr - \int_{r_{max}}^\infty \rho v_{max}^2 r_{max}^2 \frac{1}{r^3} dr = -\rho v_{max}^2 \tag{1.2}$$

where ρ is the air density. Note that the size of the vortex, as indicated by r_{max}, does not appear in the result. The hydrostatic pressure deficit beneath a convecting updraft may be computed from the overhead thermodynamic profile of the updraft column:

$$\Delta p_{hyd} = \int_0^\infty \rho' g dz = -\int_0^\infty \rho g \frac{T'}{T} dz \tag{1.3}$$

where ρ′ and T' are the density and temperature deviations in the updraft from the ambient temperature ρ and T. The assumption that the minumum pressure achievable in the vortex is due entirely to this hydrostatic presure deficit gives the thermodynamic speed limit:

$$\Delta p_{hyd} = C \rho v_{max}^2 \tag{1.4}$$

where C is some constant that depends on the vortex profile. *C=1.0* for a Rankine vortex, *C=0.5* for a stagnant core vortex [this can be seen by neglecting the first integral expression from (1.2)], and *C=0.59* for a Burgers' vortex velocity profile. Fiedler used a closed cylindrical domain, which has the advantage of preventing inflow/outflow boundary conditions from contributing to the energetics of the model. (In fact, many of the previous numerical models used fixed inflow or outflow velocities, which can act as variable energy sources.) Rather than modelling the temperature of the fluid, Fiedler used a fixed buoyancy field at the center axis of the domain to convectively drive the flow and force convergence at the lower boundary. Rotation was created by simply putting the entire domain into solid-body rotation. Fiedler (1993,1994) explored the effects of the choice of rotation rate, eddy viscosity and also the additional effect of subsidence warming in the core on the maximum windspeeds. Based on the assumption that the pressure deficit of a drowned

vortex jump can be approximated by that of a stagnant-core vortex, Fiedler (1994) observed transient vortices that exceed the thermodynamic speed limit by a factor of 5.

There is nothing about the concept or derivation of the thermodynamic speed limit which proves that it is a real constraint on the maximum velocities that can be generated in a convectively driven vortex. This is because the hydrostatic and cyclostrophic assumptions are clearly violated in the presence of substantial vertical and horizontal accelerations. Lewellen (1993) wrote: "The tornado vortex allows a significant fraction of the potential energy of the parent storm to be concentrated into wind kinetic energy where it can cause great damage." How exactly this occurs has not been completely answered.

The results of axisymmetric tornado-like vortex models have been strongly confirmed by the first detailed observations of the tornado vortex core reported by Wurman, et al. (1996) using the most recent advances in Doppler radar technology. Their observations of a tornado near Dimmit, Texas during the VORTEX field program (Rasmussen, et al. 1994), showed maximum windspeeds of over 70 ms^{-1} occurring less than 200 meters above the ground in a tight ring around the center of the tornado. The structure of the azimuthal wind field they observed was very consistent with those generated by the simulations of Howells, et al. (1988), Fiedler (1993, 1994), and also with the results we are about to show.

In this study we will examine not only the maximum windspeeds of axisymmetric tornado-like vortices, but also how the three parameters that characterize the flow - the buoyancy forcing, the rotational forcing, and the eddy viscosity - determine these windspeeds as well as the structure and behavior of the vortex. We will introduce an internal measure of the relative values of the azimuthal and vertical windspeeds in the vortex core which is analogous to the swirl ratio (1.1), and we will use this measure as well as other observations to draw new conclusions about

tornado-like vortices. We will also examine some cases which exhibit oscillatory solutions and determine the cause of these oscillations in the vortex. Finally, the implications of our results are discussed.

2 Numerical Modelling of the Axisymmetric Navier-Stokes Equations

2.1 The equations of motion and non-dimensionalization

The incompressible Navier-Stokes equations for a constant-density, constant-viscosity fluid in cylindrical coordinates, with all azimuthally varying terms eliminated are:

$$\frac{\partial u}{\partial t} + u\frac{\partial u}{\partial r} + w\frac{\partial u}{\partial z} - \frac{v^2}{r} = -\frac{1}{\rho}\frac{\partial p}{\partial r} + \frac{\mu}{\rho}\left[\frac{\partial}{\partial r}\left(\frac{1}{r}\frac{\partial}{\partial r}(ru)\right) + \frac{\partial^2 u}{\partial z^2}\right] \tag{2.1}$$

$$\frac{\partial v}{\partial t} + u\frac{\partial v}{\partial r} + w\frac{\partial v}{\partial z} + \frac{uv}{r} = \frac{\mu}{\rho}\left[\frac{\partial}{\partial r}\left(\frac{1}{r}\frac{\partial}{\partial r}(rv)\right) + \frac{\partial^2 v}{\partial z^2}\right] \tag{2.2}$$

$$\frac{\partial w}{\partial t} + u\frac{\partial w}{\partial r} + w\frac{\partial w}{\partial z} = -\frac{1}{\rho}\frac{\partial p}{\partial z} + \frac{\mu}{\rho}\left[\frac{1}{r}\frac{\partial}{\partial r}\left(r\frac{\partial w}{\partial r}\right) + \frac{\partial^2 w}{\partial z^2}\right] + F_z \tag{2.3}$$

$$\frac{1}{r}\frac{\partial}{\partial r}(ru) + \frac{\partial w}{\partial z} = \frac{\partial u}{\partial r} + \frac{u}{r} + \frac{\partial w}{\partial z} = 0 \tag{2.4}$$

where u is the radial velocity, v is the azimuthal velocity, w is the vertical velocity, p is the pressure, F_z is a vertical forcing term (the buoyant acceleration), and μ is the viscosity. The last equation is the incompressibility condition for axisymmetric flow.

The variables in (2.1)-(2.4) are non-dimensionalized as follows:

$$(u, v, w) = U(u', v', w') \tag{2.5}$$

$$(r, z) = L(r', z') \tag{2.6}$$

$$p = Pp' \tag{2.7}$$

$$F_z = FF_z' \tag{2.8}$$

$$t = Tt' = \left(\frac{L}{U}\right)t' \tag{2.9}$$

where nondimensional variables are indicated by primes, and we have used an advective time scale in (2.9). For the moment we will postpone selection of the magnitudes of the dimensional parameters U, L, P, and F. Substitution of the scalings (2.5)-(2.9) into the momentum equations (2.1)-(2.3) results in the usual nondimensionalization of the Navier-Stokes equations, with $\mu/\rho UL = 1/Re$ (the inverse Reynolds number) multiplying the diffusion terms, $P/\rho U^2$ multiplying the pressure gradient terms, and the nondimensional parameter FL/U^2 multiplying the vertical forcing term F_z'.

Following the work of Fiedler (1993), we scale the velocities according to the thermodynamic speed limit (1.4). We choose the length scale to be the height of the domain, the forcing scale F to be the average of the dimensional forcing along the r=0 axis, $F = \langle F_z(0, z)\rangle$, and:

$$U^2 = FL \tag{2.10}$$

$$P = \rho FL \tag{2.11}$$

$$\nu = \frac{\mu}{\rho UL} = \frac{1}{Re} \tag{2.12}$$

Using these scalings, and dropping the primes on the nondimensional variables, we obtain the nondimensional equations of motion:

$$\frac{\partial u}{\partial t} + u\frac{\partial u}{\partial r} + w\frac{\partial u}{\partial z} - \frac{v^2}{r} = -\frac{\partial p}{\partial r} + \nu\left[\frac{\partial}{\partial r}\left(\frac{1}{r}\frac{\partial}{\partial r}(ru)\right) + \frac{\partial^2 u}{\partial z^2}\right] \tag{2.13}$$

$$\frac{\partial v}{\partial t} + u\frac{\partial v}{\partial r} + w\frac{\partial v}{\partial z} + \frac{uv}{r} = \nu\left[\frac{\partial}{\partial r}\left(\frac{1}{r}\frac{\partial}{\partial r}(rv)\right) + \frac{\partial^2 v}{\partial z^2}\right] \tag{2.14}$$

$$\frac{\partial w}{\partial t} + u\frac{\partial w}{\partial r} + w\frac{\partial w}{\partial z} = -\frac{\partial p}{\partial z} + \nu\left[\frac{1}{r}\frac{\partial}{\partial r}\left(r\frac{\partial w}{\partial r}\right) + \frac{\partial^2 w}{\partial z^2}\right] + F_z \tag{2.15}$$

$$\frac{1}{r}\frac{\partial}{\partial r}(ru) + \frac{\partial w}{\partial z} = \frac{\partial u}{\partial r} + \frac{u}{r} + \frac{\partial w}{\partial z} = 0 \tag{2.16}$$

2.2 Numerical integration of the Navier-Stokes equations

There are two computational challenges to numerical modelling of the equations of motion. The first is the enforcement of incompressibility, (2.16); the second is the evaluation of the non-linear advection terms in the momentum equations (2.13)-(2.15) in a manner which keeps the solution stable. Traditional methods [Rotunno (1979); Fiedler (1993)] have used the following techniques for these problems: First, the radial and vertical momentum equations are combined into a streamfunction-vorticity equation and the pressure is thereby eliminated from the problem. This, however, creates the need to calculate the streamfunction from the vorticity, which has many challenges, particularly the extrapolation of the (unknown) vorticity to the domain boundaries. Secondly, the nonlinear terms in the streamfunction-vorticity equation are computed from an Arakawa-type Jacobian which keeps the system stable as long as the usual time step constraints are met.

We have instead used a velocity-pressure formulation. First, we consider the equations of motion as a simplified vector equation:

$$\frac{\partial \boldsymbol{u}}{\partial t} = \boldsymbol{F}(\boldsymbol{u}) - \nabla p \tag{2.17}$$

Here we have written the functional $\mathbf{F}(\mathbf{u})$ in place of the advective, diffusive, and vertical forcing terms. Since $\mathbf{u}$ is always nondivergent, so must be $\partial \boldsymbol{u}/\partial t$. We also know that an arbitrary vector

field, such as one generated by $\mathbf{F}(\mathbf{u})$, can be written as the sum of a nondivergent part and an irrotational (and divergent) part, the uniqueness of which are provided by the boundary conditions. Therefore we can conclude that for $\mathbf{u}$ to remain nondivergent, $-\nabla p$ must exactly cancel the irrotational part of $\mathbf{F}(\mathbf{u})$. Suppose we had some method for directly extracting the nondivergent part of $\mathbf{F}(\mathbf{u})$. We call this the projection $\mathbf{P}$ of $\mathbf{F}(\mathbf{u})$ onto the space of divergence-free vector fields. The equations of motion can then be succintly written $\partial u/\partial t = P[F(u)]$. The theory and technique behind this method were introduced by Chorin (1968, 1969) and have been developed extensively since then [see, for example, the text by Peyret and Thomas (1983)]. Most recent projection methods are second-order accurate in space and time. In axisymmetric flows the swirling velocity v is already nondivergent and is left out of the projection.

For the nonlinear advection terms, we used a Godunov-type upwinding method developed by Colella (1987) and Bell, Colella, and Glaz (1989) which is also second-order accurate. This method approximately solves the Riemann problem in the vicinity of each gridpoint and ultimately becomes a fully explicit approximation to a Crank-Nicholson method. The interested reader may find more details in Minion (1994) and Minion (1996).

In this model, the domain is divided up into rectangular cells, with velocity information stored at the cell centers and the scalar information stored at the cell corners. The edges of the outermost cells are coincident with the domain boundaries. Most of the simulations reported here use grids that are regularly spaced in each direction, with either 64x64 gridpoints or 128x128 gridpoints. Over the course of numerous simulations, we have found that for quantities such as maximum sustained velocities, the results of 64x64 gridpoint simulations were very similar to those with 128x128 gridpoints. A complete description of this axisymmetric incompressible numerical model may be found in Nolan (1996).

3 Results and Exploration of Parameter Space

3.1 Comparison to previously reported results

We tested the model by comparing it to some previously published results, using the same type of domain, boundary conditions, and forcing. As discussed above, Fiedler (1993) used an axisymmetric incompressible flow model to investigate the formation and maximum windspeeds of vortices generated by convection in a rotating domain. He used the streamfunction-vorticity method, and modified the equations so that the domain was in solid body rotation at a dimensionless rotation rate Ω=0.2. His simulations were nondimensional, with a domain height of Z=1 and radius of R=2. This radius was chosen to be large enough so as not to influence the behavior of the vortex near r=0. Although our equations did not have a Coriolis term to represent solid body rotation, we were able to reproduce Fiedler's work by initializing the azimuthal velocity with $v=\Omega r$ and by also setting the boundaries in rotation at the same rate. We used Fiedler's (1993) buoyancy field:

$$F_z(r, z) = 1.264e^{-20[r^2 + (z-0.5)^2]} \tag{3.1}$$

The major and unreproducible difference between Fiedler's simulations and ours is that his model used a stretched coordinate system which packed the gridpoints near r=0, z=0, whereas ours was designed such that it could only have equal gridpoint separation in each direction. He used 61x61 gridpoints for most of his simulations, whereas we in this case use 128x128. Finally, we also begin with the same value for the nondimensional kinematic viscosity [the inverse Reynolds number], ν=0.0005.

Figure 2 shows the vertical velocities, azimuthal velocities, pressure, and the velocity vectors in the r-z plane at t=10 for a simulation based on Fiedler's (1993) conditions. The velocity vectors in the r-z plane are hereafter referred to as the meridional velocity vectors. Figure 3 shows

these fields at t=40 (these times were chosen to compare our results to the previous work). In this later result, we can see in the meridional vector velocity plot how the vertical flow in the vortex core separates from the r=0 axis, and we can also see in the vertical velocity contour plot the appearance of a recirculation zone above the vortex core, as indicated by the negative velocities just above the surface. This feature is generally interpreted to be an axisymmetric equivalent of the vortex breakdown seen in the laboratory experiments (c.f. Figure 1). The maximum velocities and minimum pressure occurring in the domain as a function of time are shown in Figure 4. This pressure is purely dynamic and is defined to be zero in the upper-right hand corner of the domain. One can see a pattern where all three velocities episodically increase and then decrease in time. Longer simulations (not shown) revealed that these oscillations in the maximum velocities did not decay completely but periodically reappeared for as long as the simulation with these parameters was integrated. The cause of these oscillations will be discussed further below in section 4. We found that the similarity of our results to Fiedler (1993) was qualitatively very high, while quantitatively they were fairly similar although there are significant differences in the maximum velocities. Our maximum azimuthal velocity is v_{max}=1.16, which occurs at t=11.6; for Fiedler (1993), the result was v_{max}=1.26 at time t=11.

By comparing the maximum velocities at t=10 and t=40, we are inclined to draw the conclusion that the vortex is much stronger during its intensification stage than when it has settled into a nearly steady state. For certain values of rotation rate and eddy viscosity, Fiedler (1994) observed transient maximum windspeeds as much as 5 times faster than the thermodynamic speed limit (v_{max}=1 in this case) defined by the stagnant core vortex. However, it is not likely that these transient solutions offer much guidance to the dynamics of real tornadoes, which certainly do not form when a fixed vertical forcing field is instantaneously applied to a column of air in solid body

rotation. Furthermore, since tornadoes have been observed to produce damaging winds for as long as 45 minutes, it is a quasi-steady state solution that should represent them best. With this in mind, our goal should be to focus on the dynamics of quasi-steady solutions.

3.2 The effect of the ceiling at z=1

It is reasonable to wonder to what extent the "ceiling" at $z=1$ effects the formation and behavior of the vortex at the lower surface. One may also speculate that the recirculation seen in the fully-developed vortex owes its existence, at least in part, to the ceiling. To address these concerns, we ran another simulation with the same grid spacing, but twice the domain size in the vertical direction; this required using 256 grid points in the vertical direction. The results are shown in Figure 5 for the azimuthal and vertical velocities at $t=10$ and $t=40$. Comparing these to the previous results at $t=10$ and $t=40$, as shown in Figure 2 and Figure 3, we see that these results with a higher ceiling are very similar. Note especially the appearance of a recirculation zone above the fully developed drowned vortex jump vortex at $t=40$, although it is slightly weaker in the case with the higher ceiling.

3.3 Two parameters that characterize the flow

As discussed in section 1, laboratory modellers found a correlation between the structure of the tornado-like vortex and the value of the nondimensional swirl ratio S as defined by (1.1). This swirl ratio depends on the volume flow rate of the air through the apparatus and its required rotation rate as it enters the convection zone. The conventional definition of the swirl ratio is not applicable to closed domain models such as ours and that of Fiedler (1993), because the rotation and flow rates of the fluid through the central vortex is not under the control of the modeller. However, we can instead define an "internal" swirl ratio based on the measured rotation and flow rates of the fluid through the region surrounding the vortex.

To do this, we define a control volume that surrounds the central vortex, such that the

boundaries of the control volume represent the inflow region into the vortex, the outflow region above the vortex, the surface, and $r=0$. We define the *internal* swirl ratio as:

$$S_I = \frac{r_0}{2h_0} \frac{\int_0^{h_0} \Gamma(r_0, z) dz}{\int_0^{r_0} w(r, z_0) 2\pi r dr} \tag{3.2}$$

where Γ is the circulation rV. For our simulations here we use r_0=0.25, and h_0=0.25, i.e., the control volume is a cylinder of radius 0.25 and depth 0.25, adjacent to the corner at r=0, z=0.

We shall now introduce another parameter that characterizes the flow. Recall that the motivation for Fiedler's work was to determine the maximum windspeeds that can be generated by a given buoyancy field. He considered the vertical integral along $r=0$ of the buoyancy function (3.1) to be analogous to CAPE (convective available potential energy), which is a way of expressing the potential intensity of thunderstorms from their environmental thermodynamic sounding [Emanuel (1994)]. Note also that when the background vertical density profile is a constant, the CAPE is equal to the potential minimum hydrostatic pressure divided by the density ρ, i.e.:

$$\text{CAPE} = \int_0^{LNB} g \frac{T'}{T} dz = -\frac{\Delta p_{hyd}}{\rho} \tag{3.3}$$

where LNB is the level of neutral buoyancy and $T'(z)$ is the temperature deviation from the background temperature $T(z)$ of a parcel of air rising adiabatically from the surface to the LNB. For example, the maximum integral of force time distance [integral of $b(0, z)$] for the forcing used above is 0.5. Fiedler (1993, 1994) argues that the drowned vortex jump state has a cyclostrophic pressure drop which is similar to that of a stagnant core vortex which has C=0.5, so the thermodynamic speed limit for his simulations was therefore v_{max}=1. Even when the vortex is not in hydrostatic balance, we expect from dimensional considerations that the square of the max-

imum azimuthal velocity would be proportional to the equivalent of the CAPE for our numerical model:

$$\int_0^1 b(0,z)dz = Cv_{max}^2 \tag{3.4}$$

where C is some coefficient that may also depend on the viscosity and the rotational forcing. As discussed in section 1, this coefficient has certain well known values for various idealized velocity profiles. However, this C is not so easily interpreted since, for a given convective forcing, it is proportional to the inverse of the square of the maximum azimuthal velocity. We define a new *velocity coefficient* C_v as:

$$C_v = \frac{v_{max}}{\left(2\int_0^1 b(0,z)dz\right)^{1/2}} \tag{3.5}$$

By this definition, C_v is the ratio of the maximum swirling velocity to the maximum convective velocity predicted from the equivalent CAPE, i.e., $C_v = v_{max}/w_{CAPE}$.

Figure 6 shows the internal swirl ratio S_I and the velocity coefficient C_v during the original Fiedler (1993) type simulation described above. S_I is initially not well-defined since no meridional flow exists at t=0; however, as the vortex forms it quickly adjust to values which are representative of the flow under consideration. Around t=10 S_I wildly oscillates around a value of approximately 2.5 in a manner similar to the maximum vertical velocites (see Figure 4); as the vortex settles into a quasi-steady state these oscillations persist with much smaller magnitudes and a seemingly constant frequency. Around t=10 C_v shows large oscillations about a value of 0.7, but then settles into a nearly constant value of 0.8. This constancy is surprising in contrast to the oscillations in S_I, and it indicates that even while the ratio of the volumetric flow through the vortex

core to the angular momentum entering the vortex core is varying in time, the maximum azimuthal velocity is nearly constant.

It should be noted that the value of S_I also depends explicitly on the choice for the dimensions of the control volume defined above. S_I was found to have higher values for larger control volumes and lower values for smaller control volumes. Thus this internal swirl parameter is not universal in any way and cannot be compared to the swirl ratios measured in laboratory models. However, we shall see that this particular definition of the swirl ratio will be useful in the same way as the swirl ratio defined for laboratory models.

3.4 Vortex structure and intensity as a function of the controlling parameters

We now turn to the major area of investigation of this report: how do the structure and intensity of the vortex depend on the three global parameters that determine the flow? These parameters are the strength of the convective forcing, the strength of the rotational forcing (i.e., the domain rotation rate), and the magnitude of the model eddy viscosity. To determine these relationships, we performed many numerical simulations of the type outlined above, with different values for the three controlling parameters. Due to limitations of computation time, these simulations were performed the lower resolution of 64x64 gridpoints. Sets of simulations were performed with one of the parameters varying and the other two held fixed. The simulations in all cases were integrated from t=0 to t=200, and the velocities and internal swirl ratios were recorded every 10 time steps during these simulations. The mean values and the variances of the maximum velocities and the internal swirl ratio in each case were evaluated using the last 100 time units of the simulations.

We first show the dependence of the results on the strength of the convective forcing. We varied the bouyancy forcing from 10% to 200% of its original value, i.e.:

$$F_z(r,z) = C_b \times b_F,\ C_b = 0.1, 0.2, \ldots 2.0 \tag{3.6}$$

where b_F is Fiedler's original buoyancy field (3.1). The rotation rate was Ω=0.2 and the eddy viscosity was ν=0.001. Figure 7 shows the mean values of maximum velocities as a function of the strength of the convective forcing. The linear relationship between the convective forcing and the maximum kinetic energy density of the flow is approximately verified. We also show in Figure 8 the mean values of S_I and C_v for this range of convective forcing strengths. For low values of the convective forcing coefficient, C_v is increasing slowly and S_I decreases slowly with increasing convective forcing. However, for C_b>1 the values become nearly constant and approach S_I=2.2 and C_v=0.79.

Figure 9 shows the maximum velocities as a function of the rotational forcing, with the domain rotation rate Ω varying from 0.02 to 0.4. The model eddy viscosity is held fixed at ν=0.001 and the convective forcing is again Fiedler's original forcing (3.1). We can see that for very low rotation rates the radial and azimuthal velocities are very low, while the vertical velocities are relatively high. For higher rotation rates all three velocities increase, with the vertical velocities still exceeding the azimuthal velocities by about 50%. However, for larger rotation rates the vertical velocities decrease until they are substantially less than the azimuthal velocities. Over this range of values for Ω the maximum azimuthal and radial velocities decrease only slightly. Figure 10a shows the mean values of S_I and C_v versus the rotation rate. Not surprisingly, S_I increases steadily with increasing Ω. C_v has low values for the lowest values of Ω, due to the fact that an intense vortex does not form for very low values of the swirl ratio (see Figure 1). However, for values of Ω where a vortex does form, C_v increases to a maximum of 0.88 when Ω=0.08 and decreases to 0.70 when Ω=0.4. This indicates that the efficiency with which the convective forc-

ing is converted into azimuthal wind velocity decreases for large rotation rates.

A comparison of Figure 4 and Figure 6 also shows that variations in S_I are a good indicator of variations in the vertical and azimuthal velocities in the vortex core. Thus the variance of S_I is a good indicator of the variance of the maximum velocities. Figure 10b shows the variance of S_I versus the rotation rate Ω. We can see that for values of Ω greater than 0.25 the variance increases suddenly from negligible values to values on the order of 0.5. Thus we can conclude that for rotation rates Ω>0.25 the flow in the vortex core is unsteady.

How does the flow through the vortex core differ between the low-rotation rate and high-rotation rate regimes? Figure 11 shows close-ups of the velocity fields in the vortex core for the case when Ω=0.1 (plots a and b) and also when Ω=0.4 (plots c and d). In the first case the boundary layer inflow penetrates all the way to the r=0 axis, then turns upward into a strong axial jet along the axis. It separates from the axis around z=0.4. The maximum azimuthal velocities are $V = 0.79$ and they occur at r=0.1 and z=0.23. In the second case, the boundary layer inflow also penetrates to r=0 and turns upward, but the vertical flow breaks away from the vertical axis at z=0.15. The maximum azimuthal velocity is less, occurring at r=0.12 and at the much lower altitude of z=0.08. Comparison of these two results with the illustrations of the structure of laboratory vortices as a function of swirl ratio indicate that the results with Ω=0.1 clearly reproduce a low-swirl intense vortex as shown in Figure 1b, while the results with Ω=0.4 clearly reproduce a "drowned vortex jump" as shown in Figure 1c.

The high variance of S_I when its average value is 2.5 or greater (see Figure 10) indicates that the flow in the vortex core is unsteady in this regime. Figure 12 shows a sample of the time evolution of the maximum velocities in this case. All three velocity maximums undergo steady oscillations, with the vertical velocities varying the most, as much as 20%. The period of oscilla-

tion is about 6 nondimensional time units, and the maxima in the vertical velocities leads the maxima in the radial and azimuthal velocities by about 1 time unit.

Finally we repeat this analyis varying the model eddy viscosity ν while holding the convective forcing fixed to its standard value (3.1) and the rotation rate Ω=0.2. Figure 13 shows the average maximum velocities for values of the model eddy viscosity varying from ν=0.0004 to ν=0.0022. The result is remarkable in that the maximum velocities change with increasing ν in a manner that is strikingly opposite to how it changed with increasing rotation rate. By comparing Figure 14ab to Figure 10ab we can make essentially the same observation in regards to the internal swirl ratio S_I and the velocity coefficient C_v. We thus have the important observation that increasing the eddy viscosity has the same effect on the structure of the vortex as decreasing the domain rotation rate, and vice versa. Examination of the flows through the vortex core in the high and low eddy viscosity cases (not shown) gave nearly identical results to the low and high domain rotation rate results (respectively) shown in Figure 11, confiriming this observation. For the ranges of these parameters where an intense vortex is present, C_v changes relatively little. Furthermore, we see that in both cases the onset of unsteady flow in the vortex core (as measured by the variance of S_I) occurs when S_I reaches a value of approximately 2.3.

4 Analysis

We have seen how, under simple convective forcing that causes convergence, a region of fluid in solid-body rotation collapses into an intense vortex near the surface. The highest azimuthal velocities occur during the development of the vortex, which then settles into a quasi-steady state with maximum velocities determined primarily by the strength of the convective forcing. Clearly, there are two issue that call for further investigation: 1) What is the source of the

oscillations observed in the maximum velocities for certain ranges of the parameters? 2) What are the physical reasons for the relationships we have observed, particularly the apparently reciprocal relationship between the effect of changing the rotational forcing and changing the eddy viscosity? We will address the former issue first.

4.1 Examination of the oscillations in the vortex core

In section 3.4 we saw that for large values of domain rotation rate, and/or low values of the eddy viscosity, the flow through the vortex core is unsteady. Figure 12 showed that this unsteadiness is associated with steady (in some cases) oscillations in the values of the maximum velocities. What is the cause of these oscillations? Why are they not present in the low-swirl case?

To address these questions we first examined closely the velocity fields in the vortex core in the oscillatory regime. To achieve this, we ran a 64x64 gridpoint simulation, with Ω=0.4 and ν=0.001, from t=0 to t=213. We recorded the full velocity fields at 0.5 time unit intervals for the last 13 time units of the simulation. We then averaged the 26 fields to obtain an "average" state of the vortex during the oscillations. This allowed us to then derive deviations from this average state. Upon examination of these perturbation velocity fields, we observed axisymmetirc disturbances propagating down from above into the vortex core, which are shown in Figure 15 and Figure 16 in terms of the perturbation meridional vector velocity fields. In Figure 15a, we can identify a clockwise circulation centered in the vicinity of r=0.1, z=0.25. 0.5 time units later, in Figure 15b, this circulation can be seen to have moved downward slightly and is more distinct. This trend continues in the next two frames, and in Figure 15d at t=202 we can also see the beginnings of a reverse (counterclockwise) circulation appearing above z=0.3. In the next series of plots, Figure 16a-d, we can see this new circulation develop and descend until it is in approximately the same location as the original disturbance. Thus the cycle repeats itself indefinitely.

We repeated this analysis, but instead for a flow with a steady vortex core by using the same parameters as before except with Ω=0.15, which puts the vortex in the low-swirl regime, without oscillations in the vortex core. Repeating the analysis above, we show in Figure 17 a series of deviations of the meridional vector velocities from the mean. In this case, we see that the perturbations are much, much weaker than those we saw before, and rather than descending towards z=0.25 where the maximum windspeeds occur, they are stationary.

Whether or not these waves propagate downwards into the location of the maximum windspeeds is determined by the group velocities of the waves relative to the vertical velocity of the flow out of the vortex. When the vertical velocities are high enough to prevent these waves from penetrating to the surface, the vortex is said to be "supercritical," much like the flow upstream of a hydraulic jump. When the waves do penetrate to the surface, the vortex is considered to be "subcritical." From these definitions, we would say that the vortex is supercritical in the low-swirl case and subcritical in the high-swirl case. In the following section we will investigate further with a numerical analysis of the stability of the flow in the vortex core.

4.2 Eigenanalysis of axisymmetric disturbances in the vortex core

The dynamics of axisymmetric (inertial) disturbances in axisymmetric swirling flows have recieved considerable attention in the field of hydrodynamic stability. Early work on the stability of swirling flows to axisymmetric disturbances were those of Rayleigh (1880), for inviscid flows, and Taylor (1923), for viscous flows, which are summarized in the subsequent texts such as Lamb (1932), Chandresekhar (1961), and Drazin and Reid (1981). In our case we are particularly interested in the dynamics of axisymmetric disturbances in a viscous axisymmetric flow with shear in the azimuthal and vertical winds. We neglect the radial wind since it is clearly much smaller than the other velocity components in the region of interest. We would like to show that the distur-

bances we observed above are indeed associated with the shear of the vertical and azimuthal winds, and that whether they reach the surface depends on their eigenvalues.

Equations for the structure and phase speed of axisymmetric disturbances in a viscous flow with shear in both the vertical and azimuthal winds were derived in section 79 of Chandresekhar (1961) for swirling flows with azimuthal velocities of the form $V(r) = Ar + B/r$ (where A and B are constants - this is the general solution for a steady viscous swirling flow between rotating cylinders). These equations describe the evolution of small disturbances of the form:

$$u'(r, z, t) = \hat{u}(r)e^{i(kz + \omega t)} \tag{4.1}$$

and so on for the perturbation azimuthal and vertical velocities. Modifying those equations for arbitrary azimuthal velocity profiles, we have a system of two equations for the perturbation velocity functions $\hat{u}(r)$ and $\hat{v}(r)$, in a background flow with mean vertical velocity $W(r)$ and mean azimuthal velocity $V(r)$:

$$[\nu DD_* - \nu k^2 - i(\omega + kW)](DD_* - k^2)\hat{u} + ikr\hat{u}\left[DD_*\left(\frac{W}{r}\right)\right] = \frac{2Vk^2}{r}\hat{v} \tag{4.2}$$

$$[\nu DD_* - \nu k^2 - i(\omega + kW)]\hat{v} = \left(\frac{dV}{dr} + \frac{V}{r}\right)\hat{u} \tag{4.3}$$

where $D = \partial/\partial r$, $D_* = \partial/\partial r + 1/r$, and the boundary conditions are:

$$\hat{u} = DD_*\hat{u} = \hat{v} = 0 \text{ at } r = 0 \tag{4.4}$$

$$\hat{u} = D\hat{u} = \hat{v} = 0 \text{ at } r = R \tag{4.5}$$

This eigenvalue problem for ω can be solved by discretizing the system such that the functions V, W, $\hat{u}$, and $\hat{v}$ are replaced by vectors of finite length, and the differential operators are replaced by

matrix representations of their usual centered finite-difference approximations. By writing the perturbation vectors as a single state vector $\mathbf{x}$:

$$\mathbf{x} = \begin{bmatrix} \mathbf{u} \\ \mathbf{v} \end{bmatrix} \tag{4.6}$$

the system of equations (4.2)-(4.5) may be reduced to a single discrete eigenvalue problem:

$$\mathbf{A}\mathbf{x} = \omega\mathbf{B}\mathbf{x} \tag{4.7}$$

which can be solved with standard generalized eigenvalue routines.

The mean flows $V(r)$ and $W(r)$ were acquired from radial profiles of the average azimuthal and vertical velocity fields described in section 4.1, for both the high-swirl case with Ω=0.4 and the low-swirl case with Ω=0.15. We used the radial profiles of velocity at z=0.31 since the axisymmetric disturbances appeared to be very robust at this altitude. These profiles are shown in Figure 18. We first chose k=15.7, which corresponds to a vertical wavelength of 0.4, our best estimate for the axisymmetric disturbances identified above. We set the viscosity to be the same as in the numerical simulation, ν=0.001.

We did not find any unstable modes at this or any nearby wavelengths. In fact, the dissipation rates for all the modes are surprisingly high, with the imaginary parts of their eigenvalues being on the order of 0.5. The structures with the lowest dissipation rates are not similar to the axisymmetric disturbances identified above, but rather reside far away from the axis in the most quiescent part of the flow. However, we were able to identify modes which are similar to the disturbances we are looking for by selcting the one with the largest perturbation radial velocities $\hat{u}(r)$ in the vicinity of r=0.1. This mode is shown in Figure 19, and compares well to the disturbance shown in Figure 15b.

While we have not identified the source of these disturbances as spontaneously growing

unstable modes in the vortex core, some useful information can be found by examination of the phase speds and group velocities of these modes in the high- and low-swirl cases. Figure 20 shows plots of the phase speed $c_p = -\omega/k$, decay rates $\mathrm{Im}\{\omega\}$, and the real parts of the eigenvalues ω, as a function of vertical wavenumber for the two examples. The group velocity $c_g = -d\omega/dk$ may be inferred from the plots of the $\mathrm{Re}\{\omega\}$. We see that in the high-swirl case, the modes with k=15.7 have a phase speed of -0.18 and a group velocity of +0.07. In the low-swirl case, the phase speed is -0.05 and the group velocity is +0.15. Thus we can see that the tendency for linear disturbances to travel down the vortex core and reach the surface is much less in the low-swirl case than in the high-swirl case. While modes with downward group velocities were present for all wavenumbers in both cases, such modes were not similar to the disturbances identified in the numerical simulations, but rather were associated with the downward recirculation outside of the vortex. Note also that Figure 20b does indicate the existence of modes near the axis with negative group velocities for wavenumbers k<12 in the high-swirl case.

4.3 The reciprocal relationship between rotation and eddy viscosity

Measurement of the "internal swirl ratio" offers a way to characterize the state of the vortex as the parameters are varied. We have seen that for values of internal swirl ratio above 2.5, the flow at the vortex core is highly oscillatory, with alternating periods of strong and weak meridional flow through the vortex core. The internal swirl ratio, and the behavior of the vortex, appears to remain constant for a wide range of convective forcing strengths, which indicates that increasing the magnitude of the buoyancy forcing increases the wind speeds, but does not significantly change the flow structure in the vortex. We have also observed that varying the eddy viscosity has an effect on the vortex flow that is reciprocal to the effect of varying the rotational forcing - that is, increasing the viscosity has an effect similar to decreasing the rotation.

To further explore the apparently reciprocal nature of the rotational forcing and the eddy viscosity we performed a large number of 64x64 resolution simulations with varying values of both Ω and ν. Through the use of the Cray T3E at the National Energy Research Scientific Computing Ceneter (NERSC), we were able to efficiently produce an ensemble of 120 simulations with varying parameters. We found mean values and variances of the velocities, the internal swirl ratio, and the velocity coefficient for the parameter space defined by Ω=0.06,0.09...0.33, and ν=0.0006,0.0007...0.0017. The results are depicted in Figure 21, Figure 22, and Figure 23, which show the values of the mean internal swirl ratio, the mean velocity coefficient, and the variance of the internal swirl ratio, respectively, as functions of Ω and ν.

If the structure of the vortex did indeed depend solely on the ratio of the rotation rate to the eddy viscosity, then we would expect the swirl ratio to be purely a function of the ratio of these two parameters, i.e.:

$$S_I = S_I(\Omega/\nu) \tag{4.8}$$

If this were the case, then S_I would have constant values on rays emanating from the origin of the Ω-ν plane. For the most part, this is indeed what Figure 21 indicates. There are two caveats: 1) Examination of the contours of S_I showed that they did not extrapolate exactly back to the origin, but rather to a point where ν=0 and Ω has a small positive value. 2) One can clearly see that the hypothesized dependency for S_I breaks down for large values of Ω and small values of ν.

For the present we can only speculate as to the cause of these anomalies. The relationship we have discovered may after all only be approximate. The structures of the solutions may also have an additional dependence on the Reynolds number itself as defined by the convective forcing and the eddy viscosity in (2.10) and (2.12). Indeed, the results shown in Figure 8 do suggest a weak dependence of S_I on the Reynolds number. We also note that the deviations from (4.8) for

large Ω and ν are also associated with unsteady flow in the vortex core, as shown in Figure 23. The relationship may break down due the unsteadiness of the solutions in this regime. We must also consider the possibility that the solutions are under-resolved by the model in these cases.

We can offer a hypothesis as to why the curves of constant S_I do not extraploate back to the origin. Grid-based numerical models of the Navier-Stokes equations generally have a small amount of built-in numerical viscosity which effectively increase the actual viscosity of the model. If we take this additional viscosity into account the lines of constant S_I may indeed trace back to the origin where the true viscosity is zero.

The results in Figure 22 for the velocity coefficient C_v show a more complicated structure. The maximum azimuthal velocities increase both for decreasing Ω *and* decreasing ν, and for each value of ν, there is a particular value of Ω which produces the highest azimuthal velocities. We should note, however, the high azimuthal velocities indicated in the very lower left corner of the domain are not particularly meaningful in regards to tornado-like vortices. Examination of the solutions in this regime showed that an intense, near-surface vortex had not formed in these cases - the solutions were similar to the low swirl ratio, no near-surface vortex results of the laboratory experiments as depicted in Figure 1a. Thus while large azimuthal velocities were present, they were not near the surface. Fortunately, we can use S_I as a guide to when a near-surface vortex is present. Since an intense, near-surface vortex is not present when $S_I < 1.5$, we may consider the results in this regime to be irrelevant in regards to the maximum windspeeds of tornadoes.

Along with the results of the increasing-buoyancy simulation, all the results show that the vortex windspeeds are determined by the convective forcing and the velocity coefficient, while the structure and behavior of the vortex are determined by the relative values of the rotational forcing and the viscosity. The consideration of two hypothetical experiments helps to clarify the relation-

ships we have observed. The first hypothetical experiment is similar to the one we have simulated but without rotation, i.e., imagine the forced convection of an incompressible fluid above a surface, by a fixed buoyancy field with length scale L and forcing scale F. Scaling U as before by the convective velocity scale, $U^2 = FL$, we find a single dimensionless parameter which we will call the *convective* Reynolds number: $Re_C = UL/\nu$. The second problem is the interaction of an unbounded vortex with a stationary lower surface, in which case the only two dimensional parameters are the circulation $\Gamma=rv$ of the fluid in the far field, and the kinematic viscosity ν. As earlier researchers such as Barcilon (1967), Burggraf et al. (1971) and Serrin (1972) found, these two parameters necessarily form a single dimnesionless parameter that controls the flow which is sometimes called the *vortex* Reynolds number: $Re_V = \Gamma/\nu$.

Putting these two problems together, we can see that these *two* Reynolds numbers necessarily control the flow in tornado-like vortices, which in our dimensionless model are $Re_C = 1/\nu$ and $Re_V = \Omega/\nu$. From the numerical simulations we have seen that the velocity coefficient is a function of both parameters, while the structure and dynamics of the flow (i.e, the internal swirl ratio) is apparently a function of Re_V only. Why does the structure and behavior of the flow depend so strongly on the vortex Reynolds number only? The internal swirl ratio depends on the volume rate of the flow up through the axis of the vortex, which is ultimately determined by the strength of the radial inflow in the surface boundary layer and whether or not this radial inflow penetrates to the axis at $r=0$. The surface boundary layer, in turn, can be approximated by the boundary layer beneath a potential vortex. From the "point of view" of the boundary layer, Γ and ν are the only dimensional parameters! Therefore, these parameters control the radial inflow, which in turn determines the structure and behavior of the vortex.

5 Conclusions

Our results are in general agreement with previous tornado-vortex research, with the important new observation of the controlling effect of the ratio of rotational forcing to eddy viscosity on the structure and behavior of axisymmetric tornado-like vortices. This dynamical relationship is important for two reasons. First, it unifies the results of previous papers, such as those by Rotunno (1979), Walko and Gall (1986), Howells, *et. al.* (1988), and Fiedler (1994,1995), which reported a variety of results regarding vortex structure and maximum wind speeds for a variety of values for the rotational forcing and eddy viscosity. For example, in regards to how the model parameters affected the maximum windspeeds, Fiedler (1994) reported that "The decrease in viscosity has little effect on the maximum windspeed of the most intense vortex, but has a large effect on the value of 2Ω that produces the most intense vortex. With $\nu_0=2.5\text{x}10^{-4}$, the most intense vortex occurs with $2\Omega=0.07$ ... With $\nu_0=1.25\text{x}10^{-4}$, the most intense vortex occurs with $2\Omega=0.04$ ..." Thus Fiedler observed that the maximum windspeed as a function of the rotation rate was different for different viscosities - in fact for this example the rotation rate of maximum windspeed is approximately halved when the viscosity is halved; this is indeed the relationship we have demonstrated and explained.

The second reason these findings are important is that they indicate how these vortices will behave as we increase the Reynolds number to values that apply to the atmosphere. In particular, we see two trends that are significant: 1) as the model eddy viscosity is decreased, the maximum possible windspeed (for the best choice of rotation rate) increases, and 2) less and less rotational forcing is required to achieve that maximum windspeed. This first point is significant because it means that axisymmetric models may yet produce realistic tornado windspeeds if they can be run with more "realistic" Reynolds numbers. The second point is particularly important because one

of the obvious weaknesses of current numerical tornado-vortex simulations is that they supply the vortex with a steady, symmetric, and unlimited field of rotating fluid. Our results show that as the Reynolds number is increased less and less rotation will be necessary to produce a realistic tornado vortex.

Finally, our conclusions have some interesting implications for real tornadoes and the wide variety of structures and behaviors they exhibit. Tornado aficionados are familiar with two typical tornado structures: the tight, wound-up vortex with a nearly laminar appearance (typical of waterspouts, for example), and the broad, diffuse vortex with a wide base and an extremely turbulent flow (typical of severe torndaoes in the central U.S.). In analogy with the laboratory experiments, these two cases have been recognized as vortices in the low-swirl and high-swirl regime, respectively. Our results suggest that the structure of a tornado is determined entirely by the angular momentum of the background rotating wind field and an as yet undetermined appropriate value for the turbulent eddy viscosity, which may depend on various factors such as surface roughness. Given these parameters, the maximum windspeeds will then be the proportional to the intensity of the convection that supplies the vertical forcing (the overhead thunderstorm) and to the appropriate value of the velocity coefficient C_v.

The structure and dynamics of actual tornadoes will therefore depend crucially on the details of their turbulent swirling boundary layers. This leads to the inevitable conclusion that a complete understanding of tornado vortices, that can make more precise claims for observables such as the maximum windspeeds, will require an understanding of how a fully turbulent swirling boundary layer is different from a laminar approximation.

Acknowledgements

The authors would like to thank Howard Stone and Glenn Flierl for helpful discussions regarding fluid mechanics and vortex dynamics. We would also like to thank Alexandre Chorin for his extensive advice on numerical modelling, and Michael Minion and Phil Colella for their Gudonov-method advection routines and their multigrid projection solvers. We are especially grateful to Raz Kupferman for suggesting the methods we used to generate the matrix operators and to enforce higher order boundary conditions in our analysis of axisymmetric waves in the vortex core. We also gratefully acknowledge the National Energy Research Scientific Computing Center (NERSC) for providing access to the massively parallel CRAY T3E and providing support for its use. Much of the work for this report was prepared as part of the Ph.D. thesis of D. Nolan while he was a student at Harvard University, during which he was supported by NSF Grant ATM-9216813 and NSF Grant 9623539; since Novemeber of 1996 D. Nolan has been supported by the Applied Mathematical Sciences Subprogram of the Office of Energy Research, U.S. Department of Energy, under contract DE-AC03-76SF-00098. B. Farrell was supported by NSF Grant ATM-9216813 and NSF Grant 9623539.

References

Barcilon, Albert I., 1967: Vortex decay above a stationary boundary. *J. Fluid Mech.*, **27**, pp. 155-175.

Bell, John B., and Phillip Colella, and Harlan M. Glaz, 1989: A second order projection method for the incompressible Navier-Stokes equations. *J. Comp. Phys.*, **85**, pp.257-283.

----------, and Daniel L. Marcus, 1992: A second order projection method for variable-density flows. *J. Comp. Phys.*, **101**, pp. 334-348.

Benjamin, T. Brooke, 1962: Theory of the vortex breakdown phenomenon. *J. Fluid Mech.*, **14**, pp. 593-629.

Burgers, J. M., 1948: A mathematical model illustrating the theory of turbulence. *Adv. Appl. Mech.*, **1**, pp. 197-199.

Chorin, Alexandre Joel, 1968: Numerical solution of the Navier-Stokes equations. *Mathematics of Computation*, **22**, pp. 35-47.

----------, 1969: On the convergence of discrete approximations to the Navier-Stokes equations. *Mathematics of Computation*, **23**, pp.341-353.

Church, C. R., J. T. Snow, G. L. Baker, and E. M. Agee, 1979: Characterisitics of tornado-like vortices as a function of swirl ratio: A laboratory investigation. *J. Atmos. Sci.*, **36**, pp. 1755-1776.

----------, and John T. Snow, 1993: Laboratory models of tornadoes. In *The Tornado: its structure, dynamics, prediction, and hazards.* C. Church, *et. al.*, eds. American Geophysical Union, Washington, D. C.

Colella, Phillip, 1990: Multidimensional upwind methods for hyperbolic conservation laws. *J. Comp. Phys.*, **94**, pp. 61-66.

Fiedler, Brian H., 1993: Numerical simulation of axisymmetric tornadogenesis in forced convection. In *The Tornado: its structure, dynamics, prediction, and hazards.* C. Church, *et. al.*, eds. American Geophysical Union, Washington, D. C.

----------, 1994: The thermodynamic speed limit and its violation in axisymmetric numerical simulations of tornado-like vortices. *Atmosphere-Ocean*, **32**, pp. 335-359.

----------, 1995: On modelling tornadoes in isolation from the parent storm. *Atmosphere-Ocean*, **33**, pp. 501-512.

Fiedler, Brian H., and Richard Rotunno, 1986: A theory for the maximum windpseeds in tornado-like vortices. *J. Atmos. Sci.*, **43**, pp. 2328-2340.

Harvey, J. K., 1962: Some observations of the vortex breakdown phenomenon. *J. Fluid. Mech.*, **14**, pp. 585-592.

Howells, Peter C., Richard Rotunno, and Roger K. Smith, 1988: A comparitive study of atmospheric and laboratory analogue numerical tornado-vortex models. *Q. J. Roy. Met. Soc.*, **114**, pp. 801-822.

Klemp, Joseph B., and Robert B. Wilhelsom, 1978: The simulation of three-dimensional convective storm dynamics. *J. Atmos. Sci.*, **35**, pp. 1070-1096.

Lilly, D. K., 1969: Tornado Dynamics. *NCAR Manuscript* no. 69-117.

Lugt, H. J., 1989: Vortex breakdown in atmospheric columnar vortices. *Bull. Amer. Met. Soc.*, **12**, pp. 1526-1537.

Minion, Michael Lee, 1994: *Two Methods for the Study of Vortex Patch Evolution on Locally Refined Grids*. Ph.D. thesis, Department of Mathematics, University of California at Berkeley.

----------, 1996: On the stability of Godunov-projection methods for incompressible flow. *J. Comp. Phys.*, **123**, pp. 37-58.

Nolan, David S., 1996: *Axisymmetric and Asymmetric Vortex Dynamics in Convergent Flows.* Ph.D. Thesis, Department for Earth and Planetary Sciences, Harvard University, 1996.

Peyret, Roger, and Thomas D. Taylor, 1983: *Computational Methods for Fluid Flow.* Springer-Verlag, New York.

Rasmussen, Erik N., Jerry M. Straka, Robert Davies-Jones, Charles A. Doswell III, Frederick H. Carr, Michael D. Eilts, and Donald R. MacGorman, 1994: Verification of the origins of rotation in tornadoes: VORTEX. *Bull. Am. Met. Soc.*, **75**, pp. 995-1006.

Rotunno, Richard, 1977: Numerical simulation of a laboratory vortex. *J. Atmos. Sci.*, **34**, 1942-1956.

----------, 1979: A study in tornado-like vortex dynamics. *J. Atmos. Sci.*, **36**, pp. 140-155.

----------, 1984: An investigation of a three-dimensional asymmetric vortex. *J. Atmos. Sci.*, **41**, pp. 283-298.

Serrin, J., 1972: The swirling vortex. *Phil. Trans. R. Soc. London*, **271**, pp. 325-360.

Stephens, A. B., J. B. Bell, J. M. Solomon, and L. B. Hackerman, 1984: A finite difference Galerkin formulation for the incompressible Navier-Stokes equations. *J. Comp. Phys.*, **53**, pp. 152-172.

----------, and Robert Gall, 1986: Some effects of momentum diffusion on axisymmetric vortices. J. Atmos. Sci., 43, pp. 2137-2148.

Ward, N. B., 1972: The exploration of certain features of tornado dynamics using a laboratory model. *J. Atmos. Sci.*, **29**, pp. 1194-1204.

----------, 1995: Simulation and analysis of tornado development and decay within a three-dimensional supercell thunderstorm. *J. Atmos. Sci.*, **52**, pp. 2675-2703.

Wilson, Tim, and Richard Rotunno, 1986: Numerical simulation of a laminar end-wall vortex and boundary layer. *Phys. Fluids*, **29**, pp. 3993-4005

Wurman, Joshua, Jerry M. Straka, and Erik N. Rasmussen, 1996: Fine-scale doppler radar observations of tornadoes. *Science*, **272**, pp. 1774-1777.

Figure Captions

Figure 1: Illustrations of four of the stages that laboratory and numerical models of tornados produce as the swirl ratio is increased from zero: a) weak vortex stage; b) surface vortex with vortex breakdown above the surface; c) drowned vortex jump (breakdown just above the surface); d) two-celled vortex with stagnant core. The solid lines are streamlines of meridional flow, the arrows indicate the direction and details of the circulation, and the "M" marks the location of the maximum azimuthal (swirling) velocities.

Figure 2: Results for the Fiedler (1993)-type simulation at t=10: a) Swirling (azimuthal) velocity; b) vertical velocity; c) pressure; d) meridional velocity vectors in the r-z plane. Dashed contours indicate negative values, maxima and minima are indicated, and the contour intervals are indicated at the top of each plot.All plots show the domain for $0<r<1$, $0<z<1$, except for the meridional vector velocity plot, which is for $0<r<0.3$, $0<z<0.3$.

Figure 3: Results for the Fiedler (1993)-type simulation at t=40: a) Swirling (azimuthal) velocity; b) vertical velocity; c) pressure; d) meridional velocity vectors in the r-z plane. Dashed contours indicate negative values, maxima and minima are indicated, and the contour intervals are indicated at the top of each plot. All plots show the domain for $0<r<1$, $0<z<1$, except for the meridional vector velocity plot, which is for $0<r<0.3$, $0<z<0.3$.

Figure 4: Maximum velocities and minumum pressure as a function of time in the original Fiedler (1993)-type simulation: vertical velocity (dash-dot), azimuthal velocity (dashed), inward radial velocity (solid), and pressure (solid, negative).

Figure 5: Results of a Fiedler (1993)-type siumlation with twice the domain height: a) contours of azimuthal velocity at t=10; b) contours of vertical velocity at t=10; c) contours of azimuthal velocity at t=40; d) contours of vertical velocity at t=40. The domain in each frame is from 0<r<1, 0<z<2. Dashed contours indicate negative values, maxima and minima are indicated, and the contoru intervals are indicated at the top of each plot.

Figure 6: Internal swirl ratio S_I (solid line) and velocity coefficient C_v (dashed lined) during the Fiedler (1993)-type simulation shown above.

Figure 7: Averages of the squares of the maximum velocities as a function of the strength of the convective forcing: average squared radial velocities are marked by circles, azimuthal velocities are marked by x's and vertical velocities are marked by +'s.

Figure 8: Average values for the internal swirl ratio S_I and the velocity coeffcient C_v as a function of the strength of the convective forcing; S_I is marked by the circles and C_v is marked by the +'s.

Figure 9: Average maximum velocities as a function of the rotation rate Ω: radial velocities are marked by circles, azimuthal velocities are marked by +'s, and vertical velocities are marked by x's.

Figure 10: a) Average values for the internal swirl ratio S_I and the velocity coefficient C_v as a function of the rotation rate Ω of the domain. S_I is marked by the circles and C_L is marked by the +'s; b) Variance of S_I as a function of the rotation rate Ω of the domain.

Figure 11: Close-up of the velocity fields in the vortex core for two different domain rotation rates:

a) close-up of the azimuthal velocity field for Ω=0.1; b) close-up of the meridional velocity vectors for Ω=0.1; c) close-up of the azimuthal velocity field for Ω=0.4; d) close-up of the meridional velocity vectors for Ω=0.4. The contour intervals or maximum velocities are indicated at the top of each frame.

Figure 12: A sample of the time evolution of the maximum velocities in a Fiedler (1993)-type simulation with Ω=0.4 and ν=0.001: maximum inward radial velocities (solid), azimuthal velocities (dashed), and vertical velocities (dash-dot).

Figure 13: Average maximum velocities as a function of the model eddy viscosity: average maximum radial velocities are marked by circles, azimuthal velocities are marked by +'s and vertical velocities are marked by x's.

Figure 14: a) Average values for the internal swirl ratio S_I and the velocity coefficient C_v as a function of the model eddy viscosity ν. S_I is marked by the circles and C_v is marked by the +'s; b) Variance of S_I as a function of the model eddy viscosity ν.

Figure 15: Meridional vector velocity plots of the deviations from the average velocity field of the vortex in the oscillatory, high-swirl regime: a) deviation from the mean at t=200.5; b) t=201.0; c) t=201.5; d) t=202.0. The plots show the domain from 0<r<0.5, 0<z<0.5. The maximum velocities are indicated at the top of each frame.

Figure 16: Meridional vector velocity plots of the deviations from the average velocity field of the vortex in the oscillatory, high-swirl regime: a) deviation from the mean at t=202.5; b) t=203.1; c) t=203.6; d) t=204.1. The plots show the domain from 0<r<0.5, 0<z<0.5. The maximum velocities are indicated at the top of each frame.

Figure 17: Meridional vector velocity plots of the deviations from the average velocity field of the vortex in the steady, low-swirl regime: a) deviation from the mean at t=180.0; b) t=180.5; c) t=181.0; d) t=181.5. The plots show the domain from $0<r<0.5$, $0<z<0.5$. The maximum velocities are indicated at the top of each frame.

Figure 18: Radial profiles of average azimuthal and vertical velocities at z=0.3125 in the two simulations considered in section 4.1: a) azimuthal velocity, high-swirl case; b) vertical velocity, high-swirl case; c) azimuthal velocity, low-swirl case; d) vertical velocity, low-swirl case.

Figure 19: Modal structure with vertical wavelentgh 0.4 and maximum radial velocities at r=0.1 found from eigenanalysis of the vortex core in the high-swirl case.

Figure 20: Plots of phase speed, decay rate, and the real parts of ω versus vertical wavenumber k for the modes with maximum amplitude at r=0.1: a) phase speed and decay rate, high swirl case; b) ω, high-swirl case; c) phase speed and decay rate, low-swirl case; d) ω, low-swirl case.

Figure 21: Contour plot of the mean value of the internal swirl ratio as a function of the domain rotation rate Ω and the eddy viscosity ν.

Figure 22: Contour plot of the mean value of the velocity coefficient C_v as a function of the domain rotation rate Ω and the eddy viscosity ν.

Figure 23: Contour plot of the variance of the internal swirl ratio S_I as a function of the domain rotation rate Ω and the eddy viscosity ν. Due to the wide range in values for the vari-

ance, the contour levels have been chosen arbitratily to have the following values : 0.04, 0.08...0.16; 0.2, 0.4....1.2.

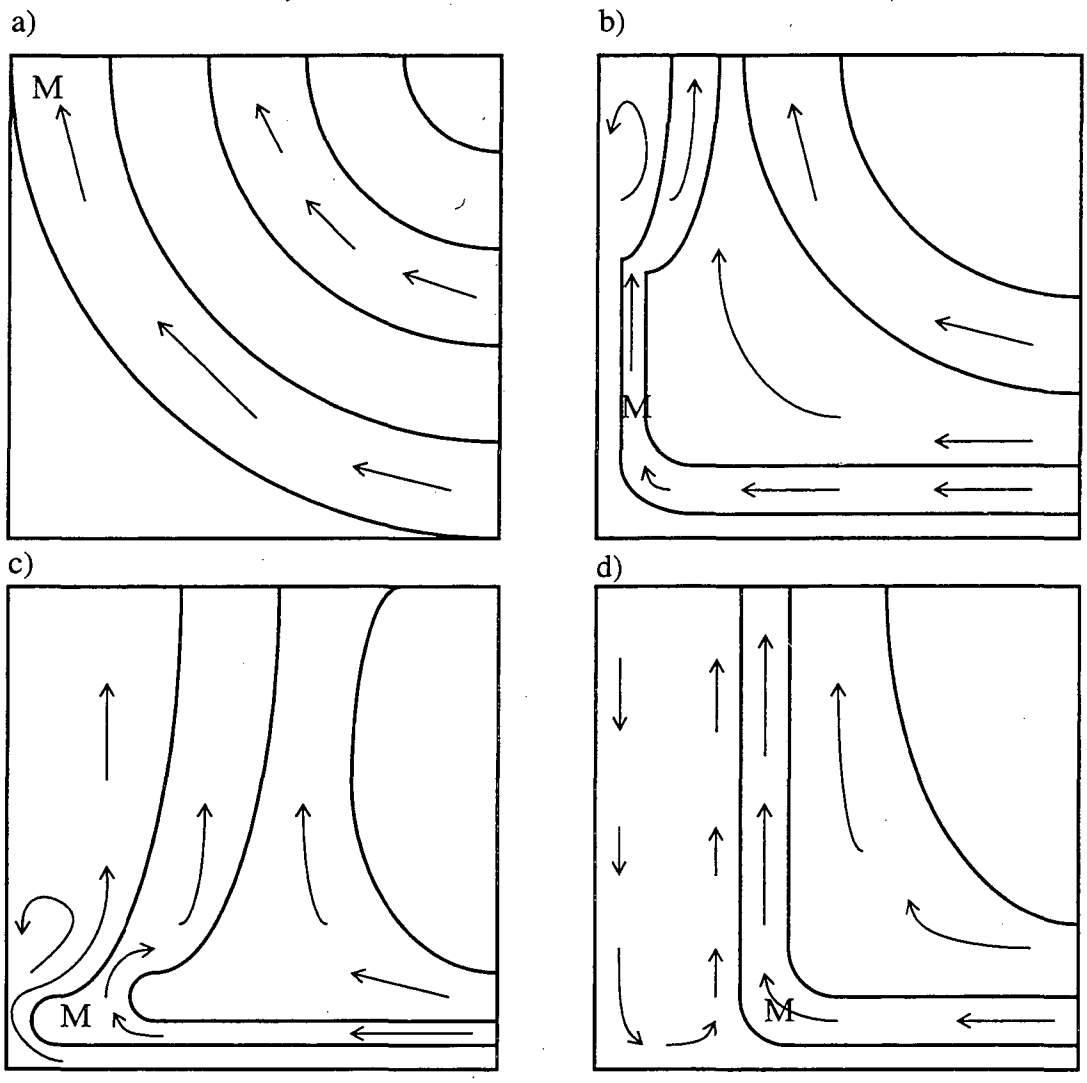

Figure 1 Illustrations of four of the stages that laboratory and numerical models of tornados produce as the swirl ratio is increased from zero: a) weak vortex stage; b) surface vortex with vortex breakdown above the surface; c) drowned vortex jump (breakdown just above the surface); d) two-celled vortex with stagnant core. The solid lines are streamlines of meridional flow, the arrows indicate the direction and details of the circulation, and the "M" marks the location of the maximum azimuthal (swirling) velocities.

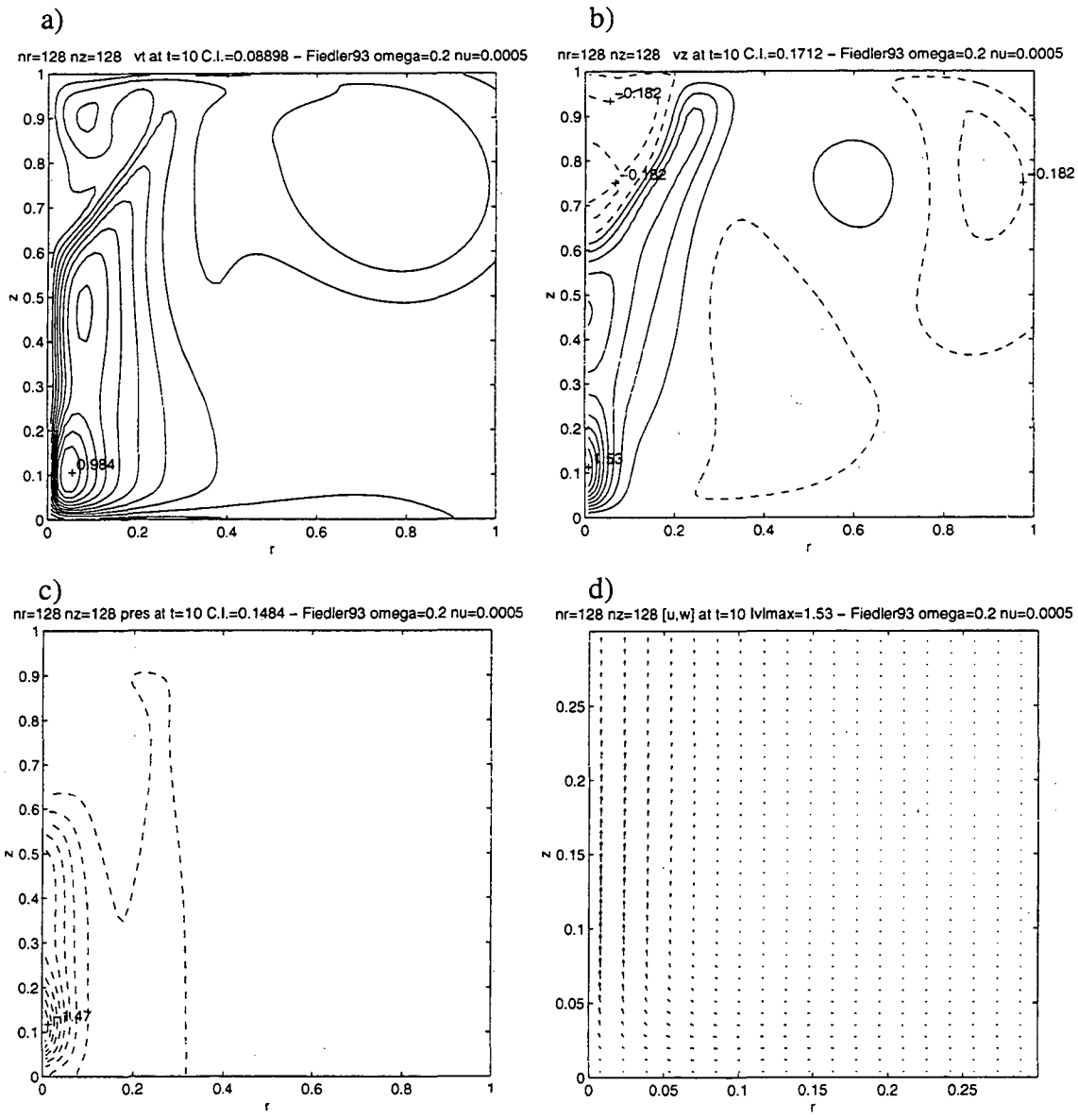

Figure 2 Results for the Fiedler (1993)-type simulation at t=10: a) Swirling (azimuthal) velocity; b) vertical velocity; c) pressure; d) meridional velocity vectors in the r-z plane. Dashed contours indicate negative values, maxima and minima are indicated, and the contour intervals are indicated at the top of each plot.All plots show the domain for $0<r<1$, $0<z<1$, except for the meridional vector velocity plot, which is for $0<r<0.3$, $0<z<0.3$.

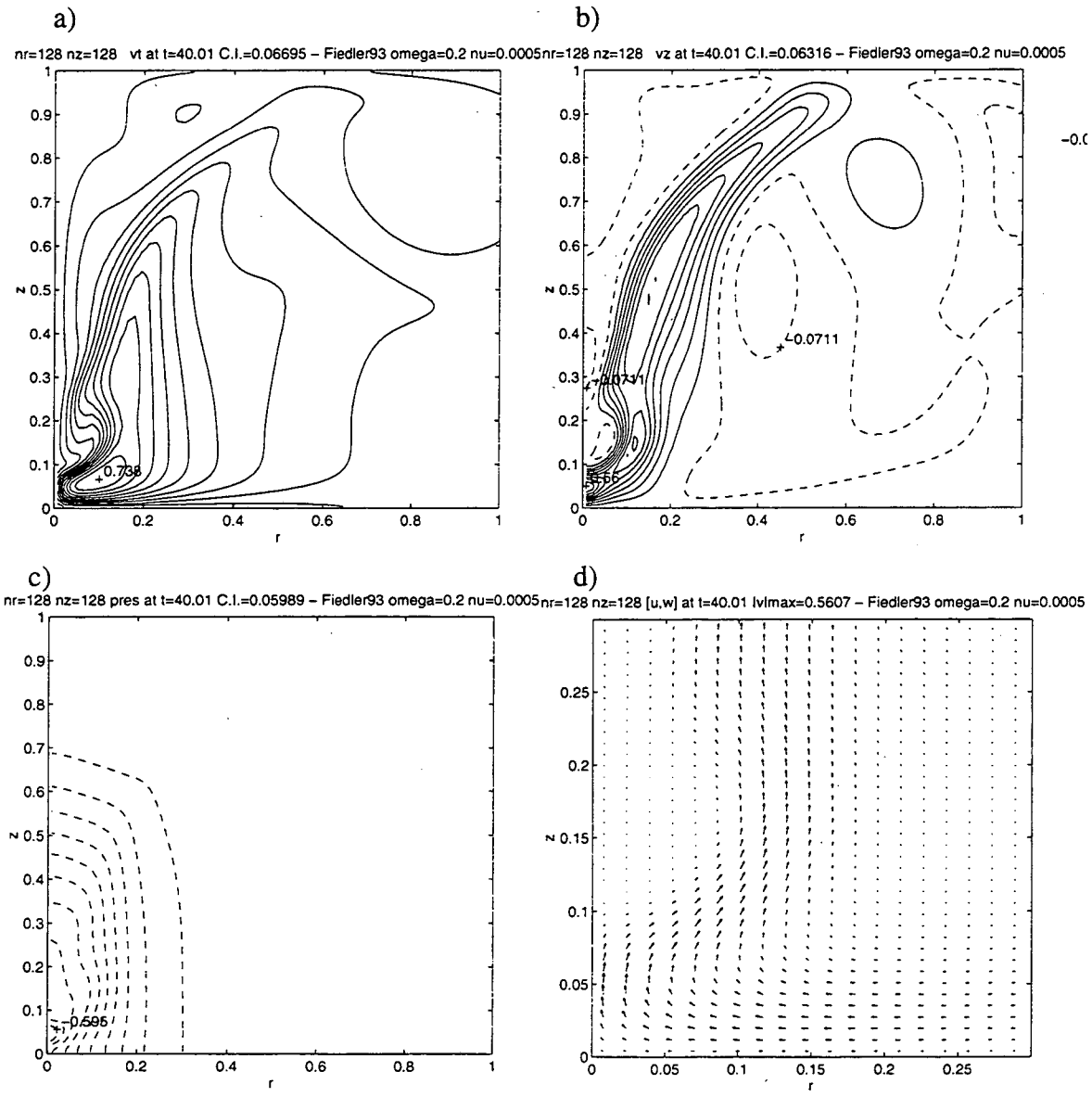

Figure 3 Results for the Fiedler (1993)-type simulation at t=40: a) Swirling (azimuthal) velocity; b) vertical velocity; c) pressure; d) meridional velocity vectors in the r-z plane. Dashed contours indicate negative values, maxima and minima are indicated, and the contour intervals are indicated at the top of each plot. All plots show the domain for $0<r<1$, $0<z<1$, except for the meridional vector velocity plot, which is for $0<r<0.3$, $0<z<0.3$.

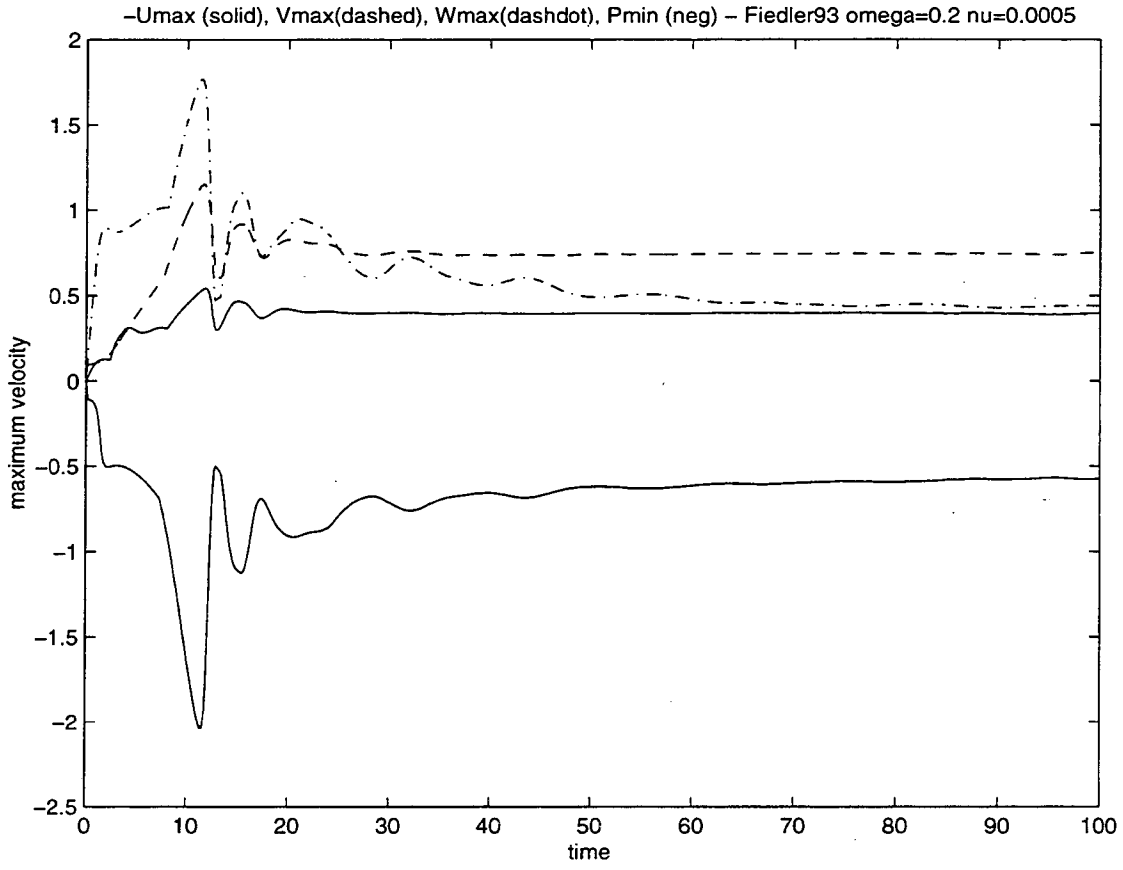

Figure 4 Maximum velocities and minumum pressure as a function of time in the original Fiedler (1993)-type simulation: vertical velocity (dash-dot), azimuthal velocity (dashed), inward radial velocity (solid), and pressure (solid, negative).

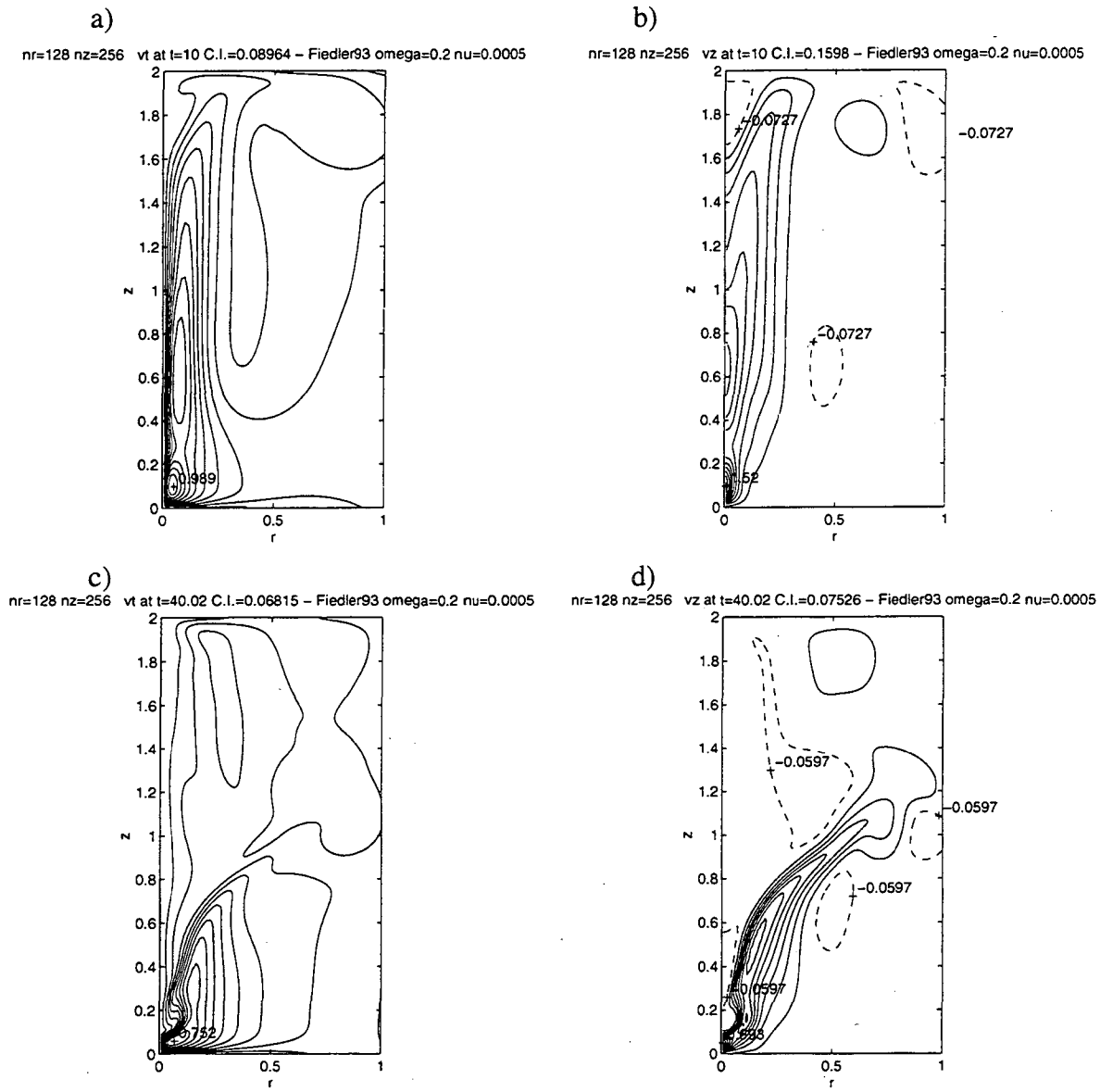

Figure 5 Results of a Fiedler (1993)-type siumlation with twice the domain height: a) contours of azimuthal velocity at t=10; b) contours of vertical velocity at t=10; c) contours of azimuthal velocity at t=40; d) contours of vertical velocity at t=40. The domain in each frame is from 0<r<1, 0<z<2. Dashed contours indicate negative values, maxima and minima are indicated, and the contoru intervals are indicated at the top of each plot.

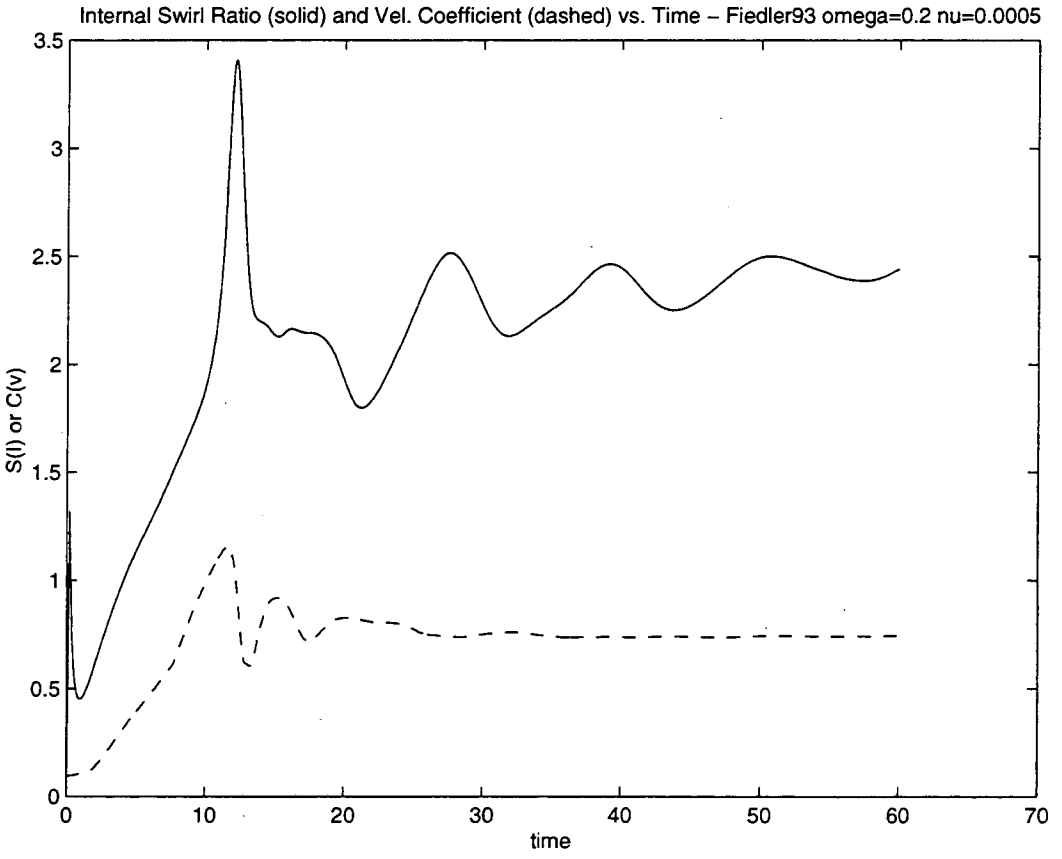

Figure 6 Internal swirl ratio S_I (solid line) and velocity coefficient C_v (dashed lined) during the Fiedler (1993)-type simulation shown above.

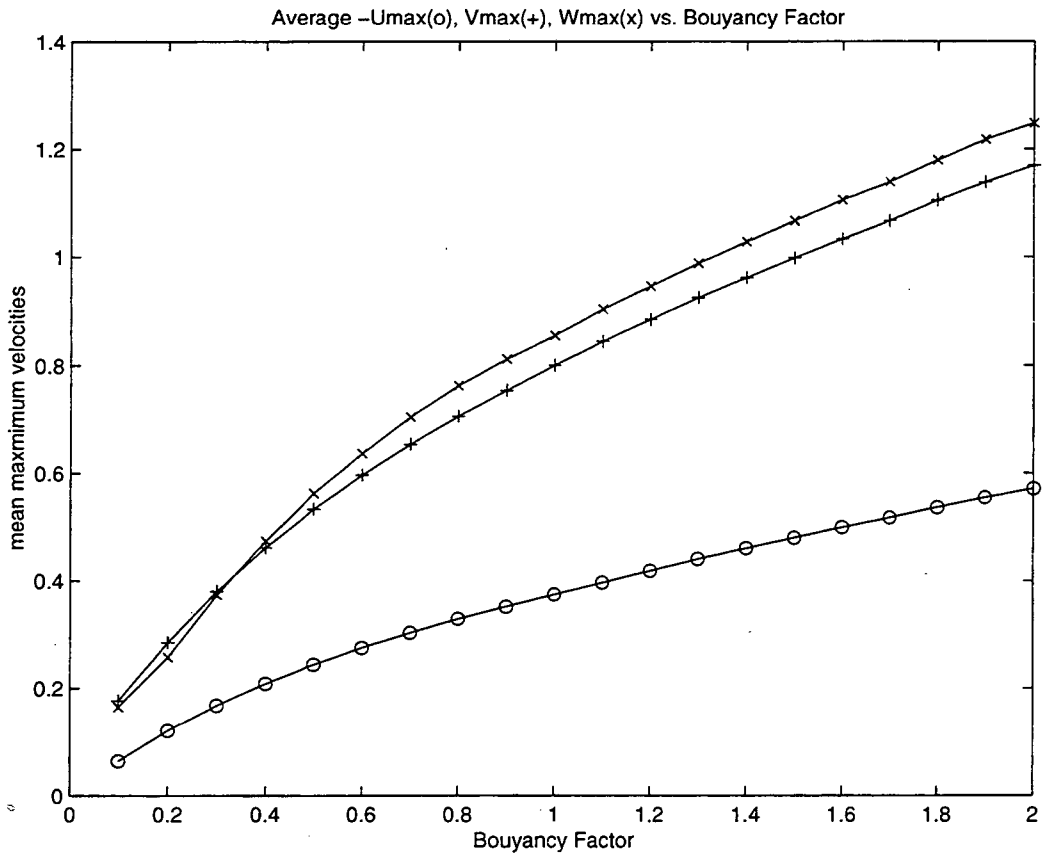

Figure 7 Averages of the squares of the maximum velocities as a function of the strength of the convective forcing: average squared radial velocities are marked by circles, azimuthal velocities are marked by x's and vertical velocities are marked by +'s.

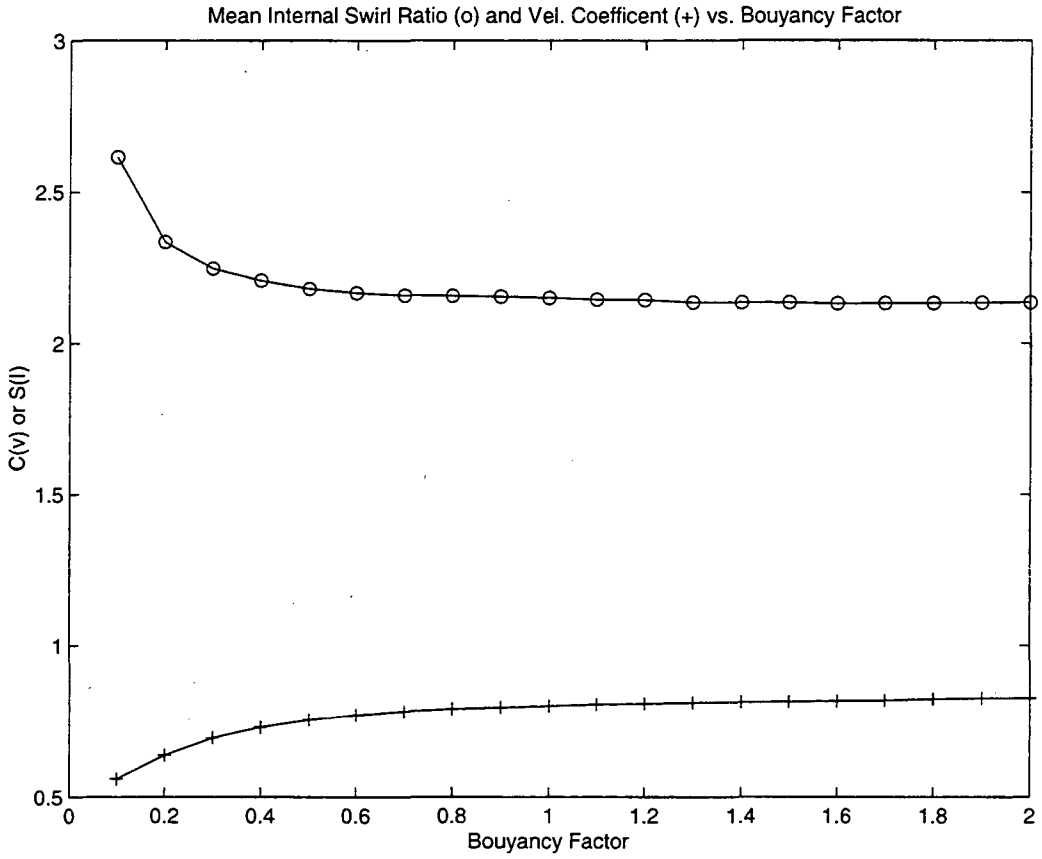

Figure 8 Average values for the internal swirl ratio S_I and the velocity coeffcient C_v as a function of the strength of the convective forcing; S_I is marked by the circles and C_v is marked by the +'s.

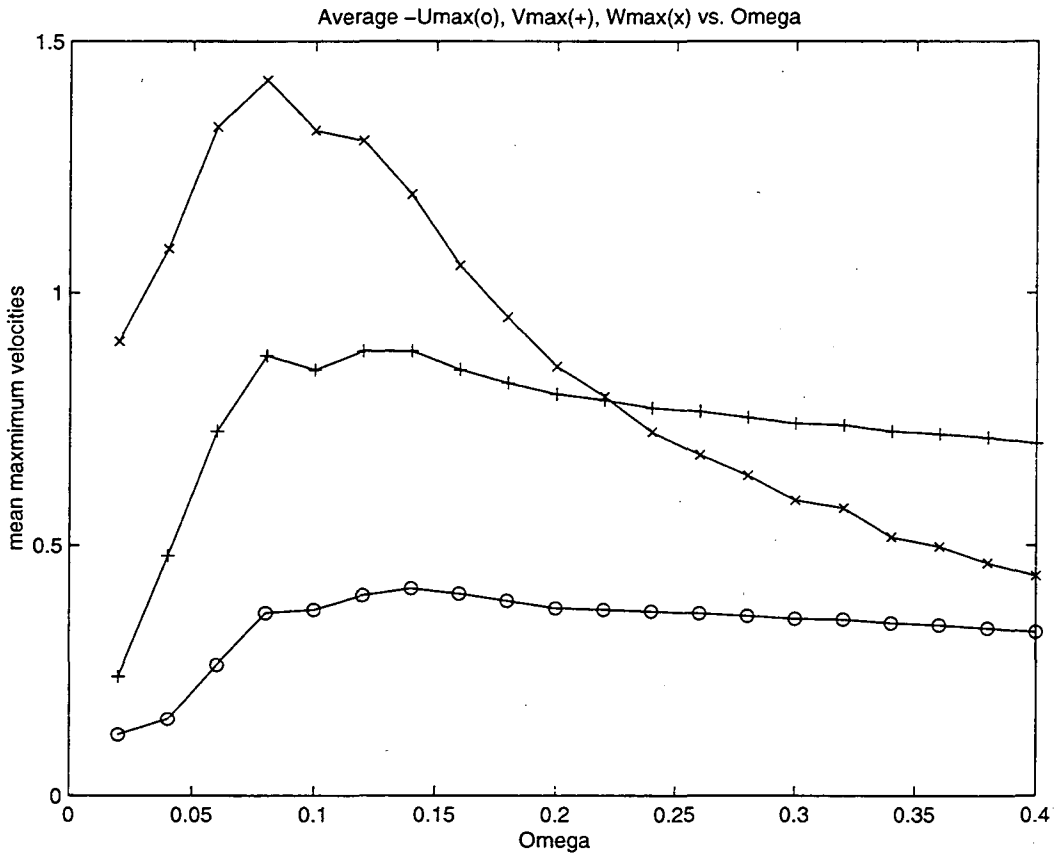

Figure 9 Average maximum velocities as a function of the rotation rate Ω: radial velocities are marked by circles, azimuthal velocities are marked by +'s, and vertical velocities are marked by x's.

a)

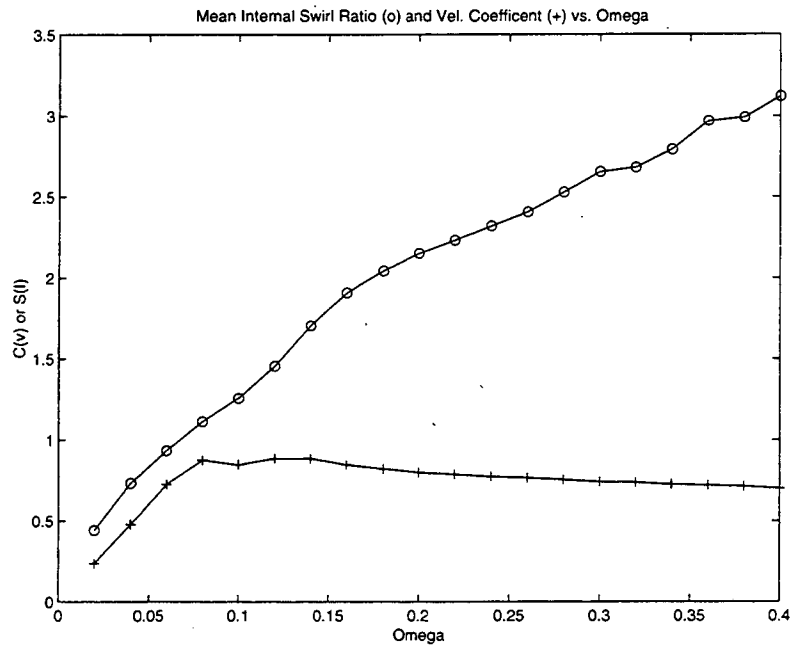

b)

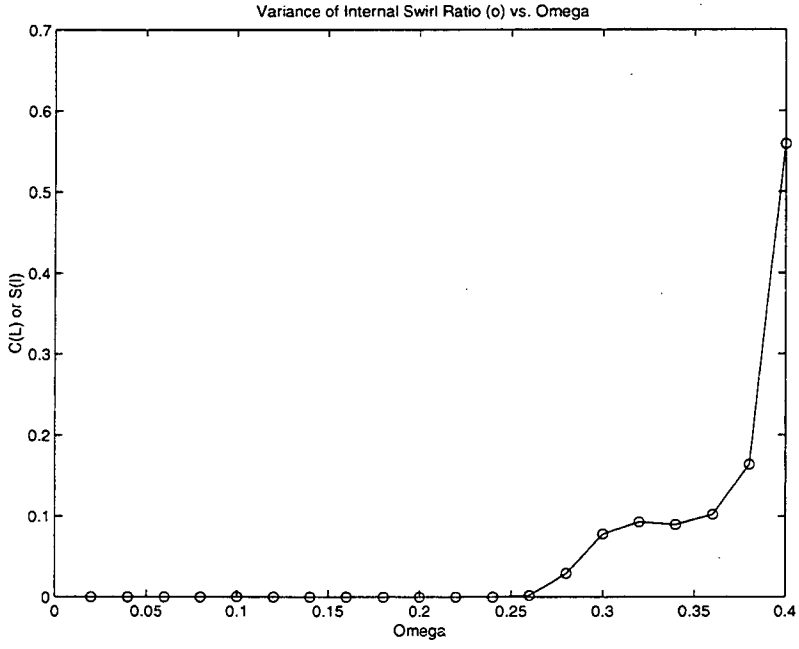

Figure 10 a) Average values for the internal swirl ratio S_I and the velocity coefficient C_v as a function of the rotation rate Ω of the domain. S_I is marked by the circles and C_L is marked by the +'s; b) Variance of S_I as a function of the rotation rate Ω of the domain.

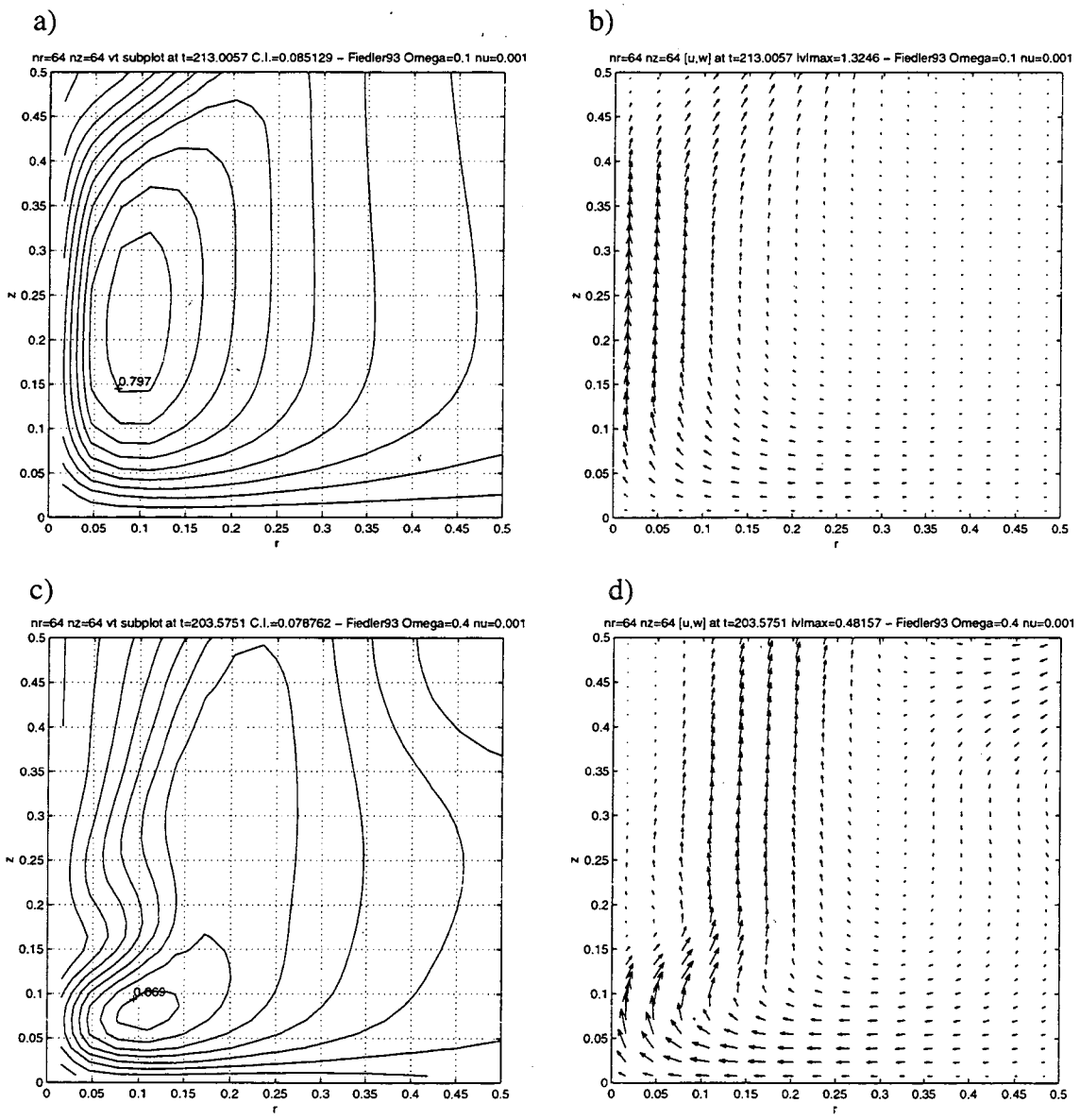

Figure 11 Close-up of the velocity fields in the vortex core for two different domain rotation rates: a) close-up of the azimuthal velocity field for Ω=0.1; b) close-up of the meridional velocity vectors for Ω=0.1; c) close-up of the azimuthal velocity field for Ω=0.4; d) close-up of the meridional velocity vectors for Ω=0.4. The contour intervals or maximum velocities are indicated at the top of each frame.

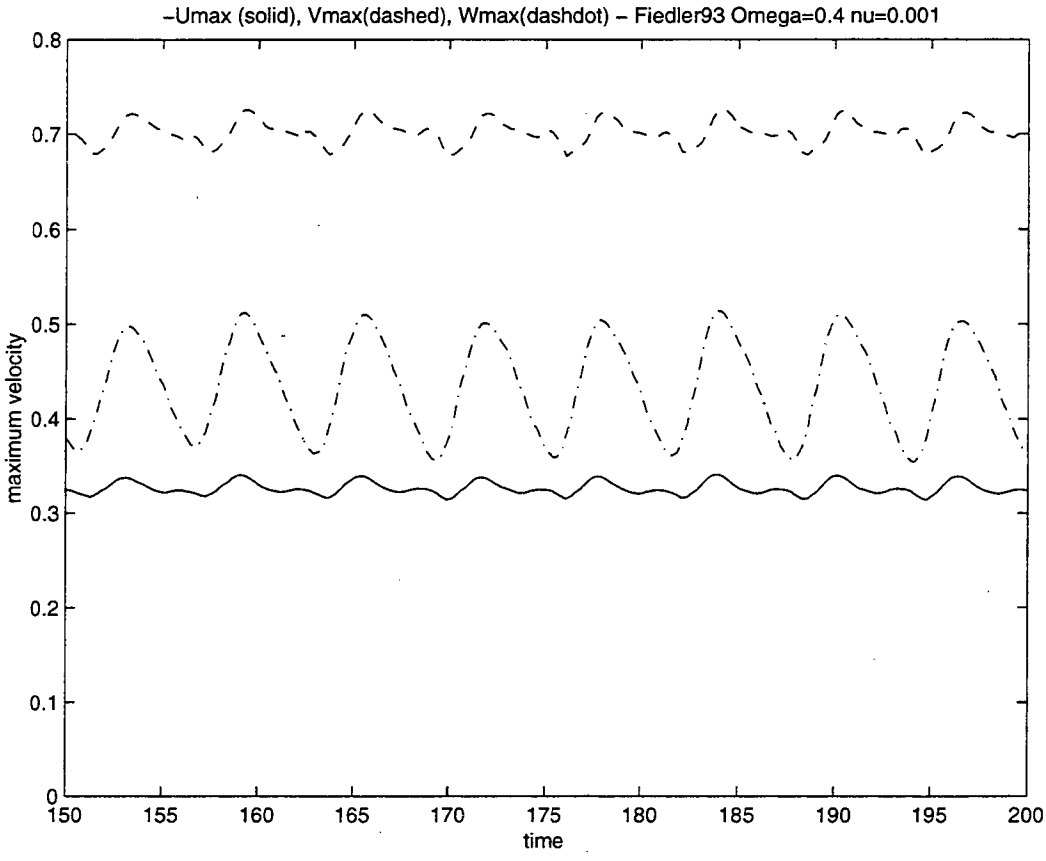

Figure 12 A sample of the time evolution of the maximum velocities in a Fiedler (1993)-type simulation with Ω=0.4 and ν=0.001: maximum inward radial velocities (solid), azimuthal velocities (dashed), and vertical velocities (dash-dot).

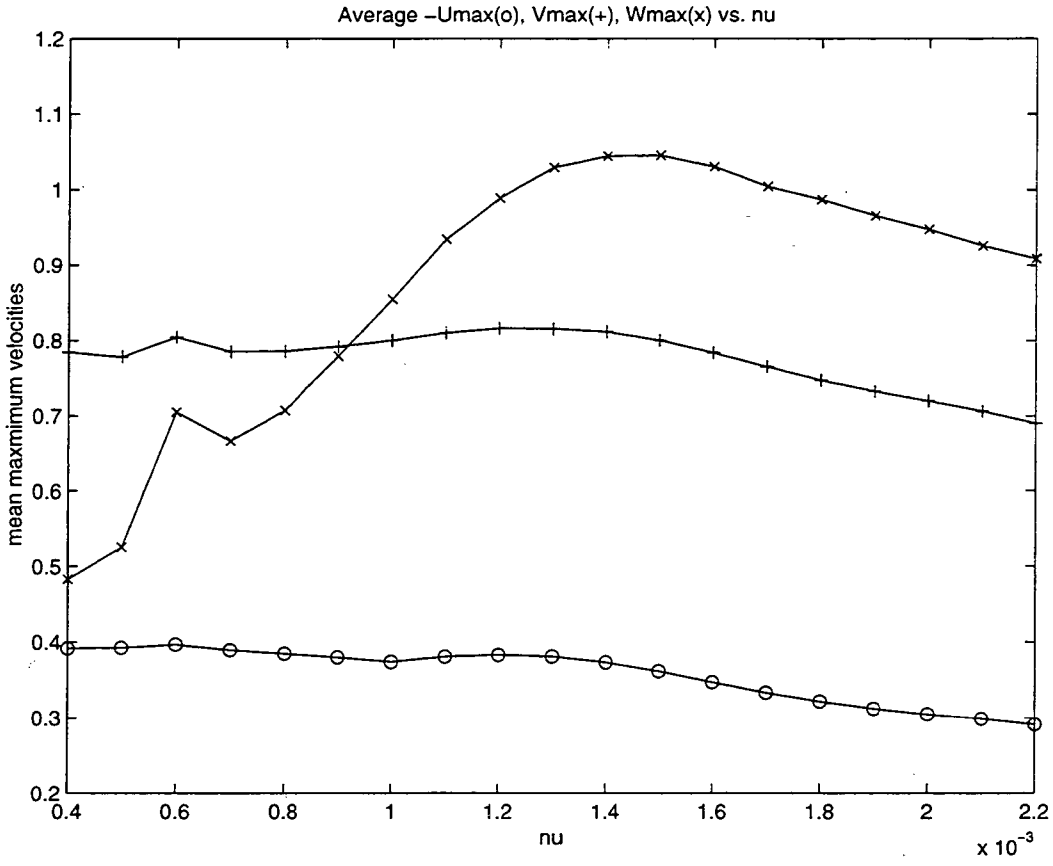

Figure 13 Average maximum velocities as a function of the model eddy viscosity: average maximum radial velocities are marked by circles, azimuthal velocities are marked by +'s and vertical velocities are marked by x's.

a)

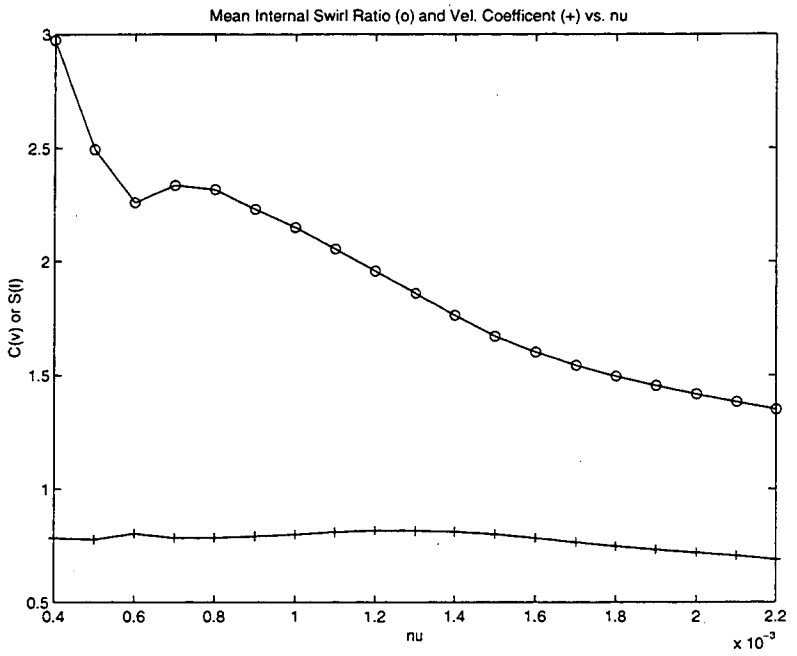

b)

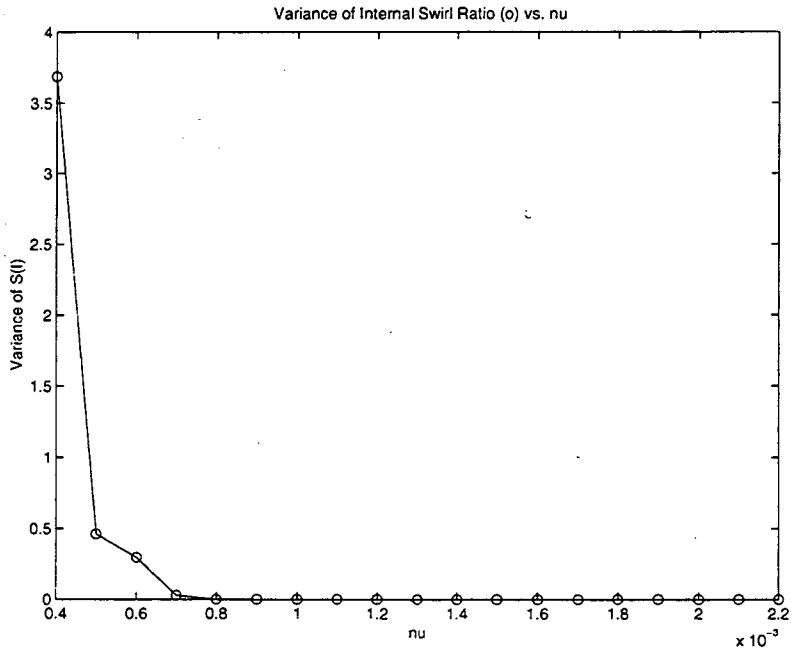

Figure 14 a) Average values for the internal swirl ratio S_I and the velocity coefficient C_v as a function of the model eddy viscosity ν. S_I is marked by the circles and C_v is marked by the +'s; b) Variance of S_I as a function of the model eddy viscosity ν.

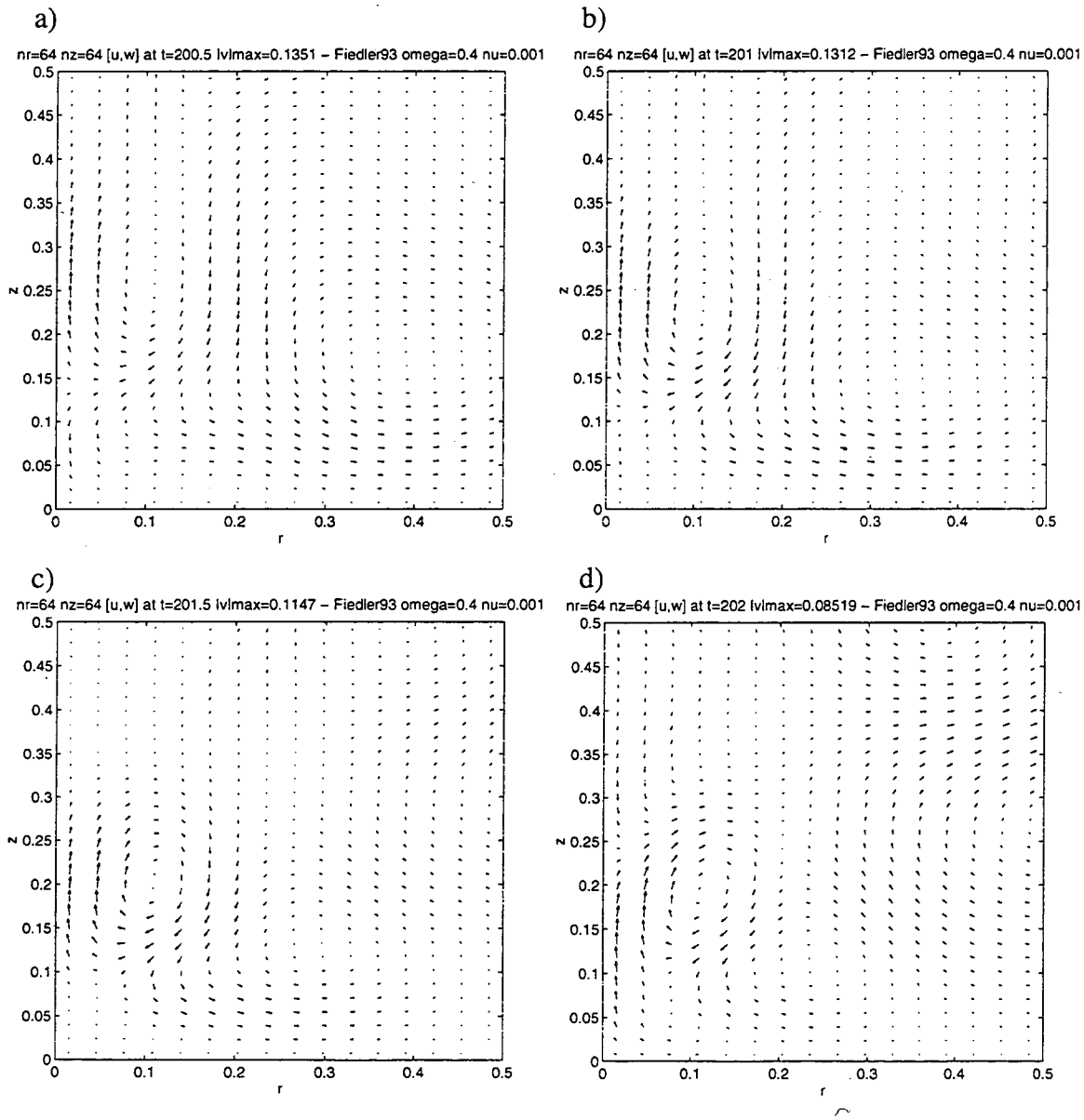

Figure 15 Meridional vector velocity plots of the deviations from the average velocity field of the vortex in the oscillatory, high-swirl regime: a) deviation from the mean at t=200.5; b) t=201.0; c) t=201.5; d) t=202.0. The plots show the domain from $0<r<0.5$, $0<z<0.5$. The maximum velocities are indicated at the top of each frame.

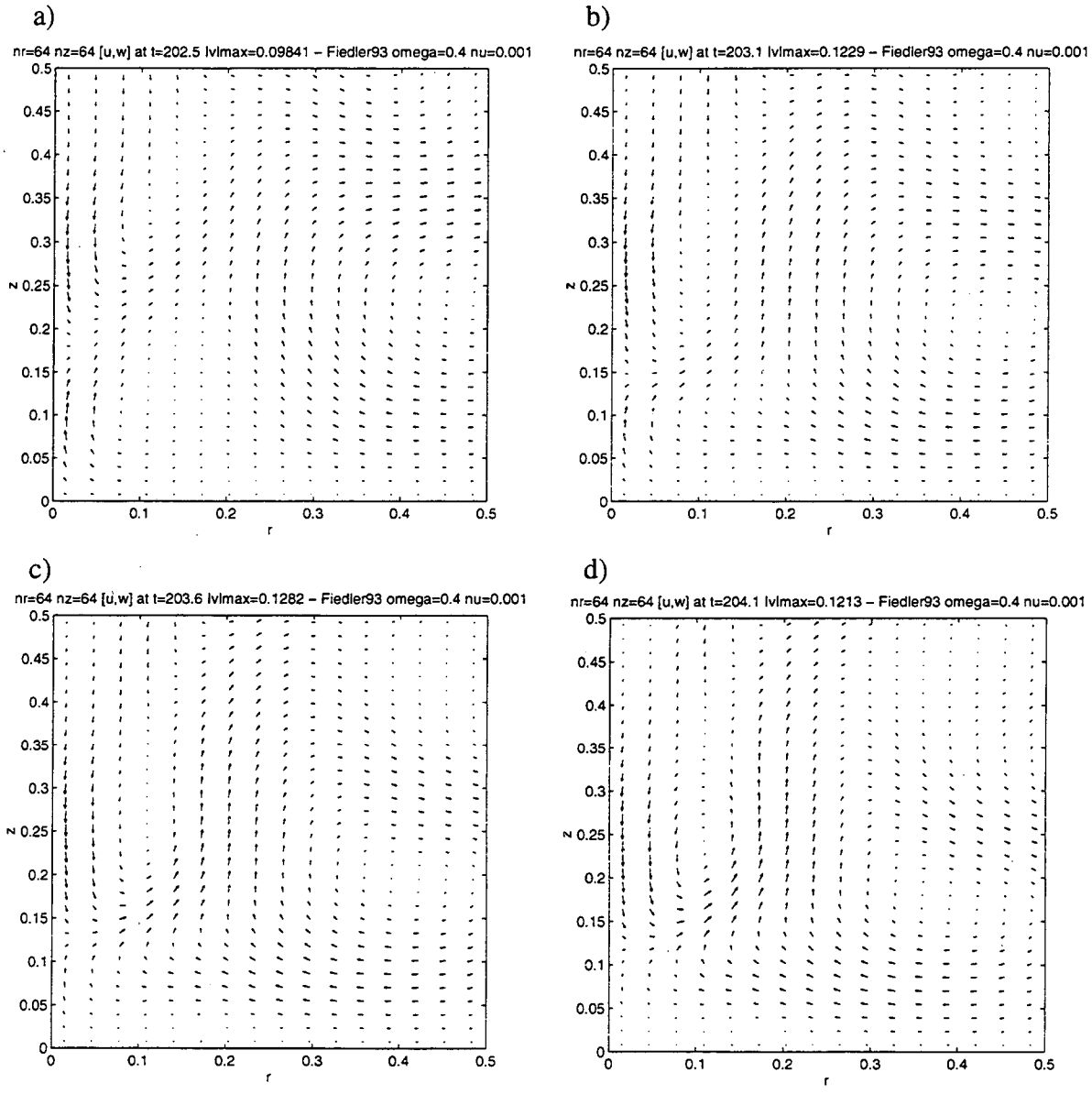

Figure 16 Meridional vector velocity plots of the deviations from the average velocity field of the vortex in the oscillatory, high-swirl regime: a) deviation from the mean at t=202.5; b) t=203.1; c) t=203.6; d) t=204.1. The plots show the domain from $0<r<0.5$, $0<z<0.5$. The maximum velocities are indicated at the top of each frame.

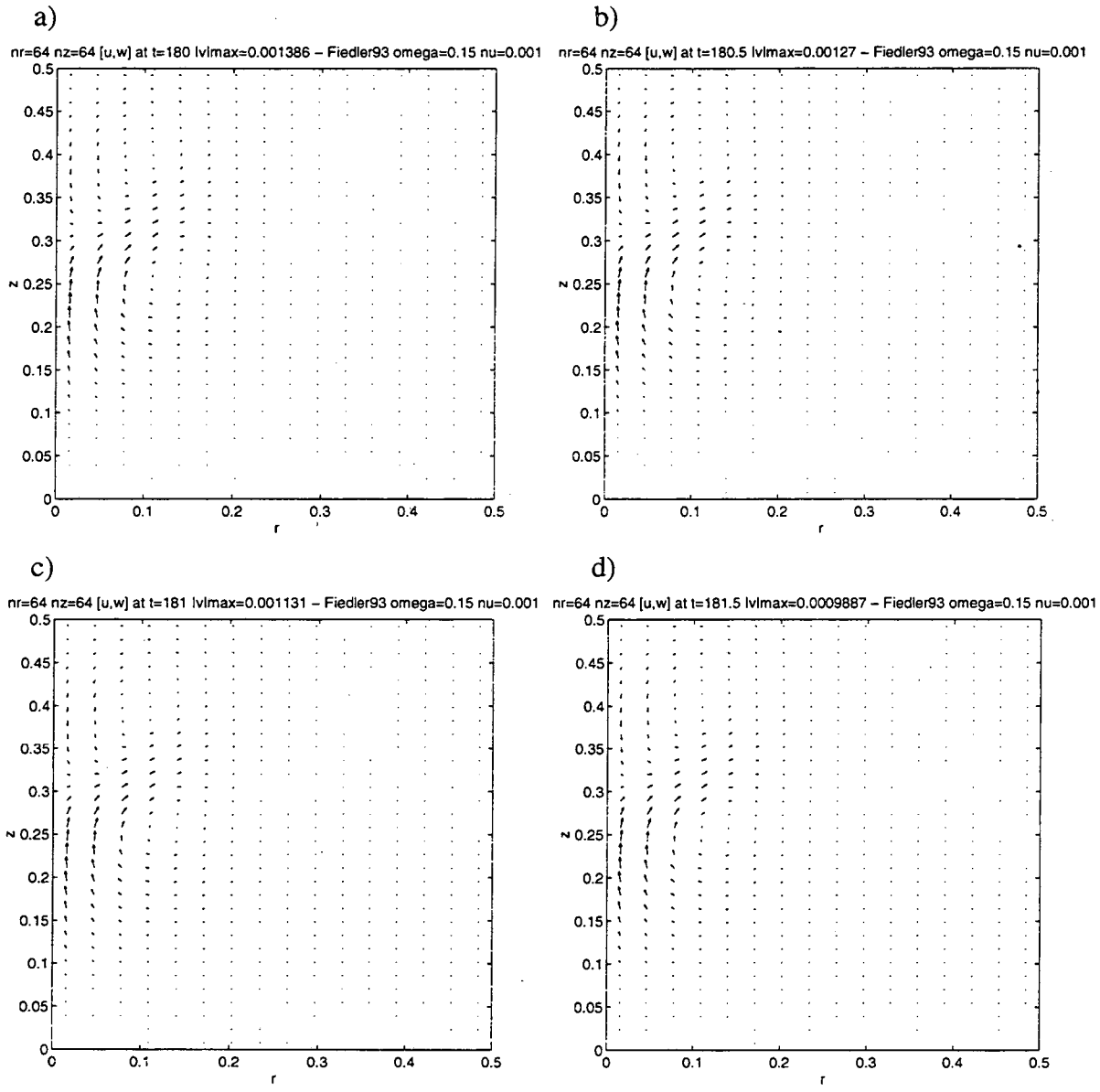

Figure 17 Meridional vector velocity plots of the deviations from the average velocity field of the vortex in the steady, low-swirl regime: a) deviation from the mean at t=180.0; b) t=180.5; c) t=181.0; d) t=181.5. The plots show the domain from $0<r<0.5$, $0<z<0.5$. The maximum velocities are indicated at the top of each frame.

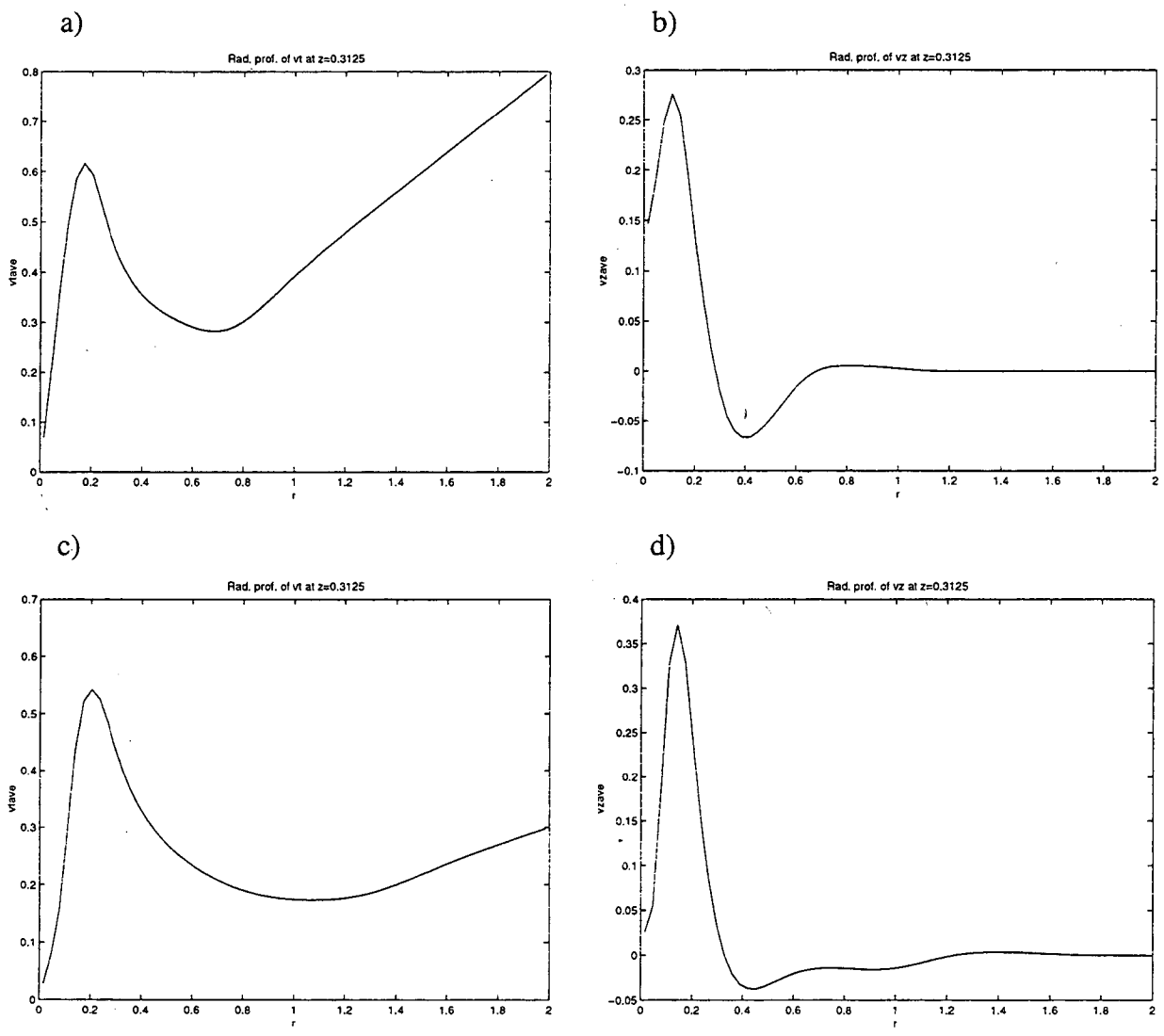

Figure 18 Radial profiles of average azimuthal and vertical velocities at z=0.3125 in the two simulations considered in section 4.1: a) azimuthal velocity, high-swirl case; b) vertical velocity, high-swirl case; c) azimuthal velocity, low-swirl case; d) vertical velocity, low-swirl case.

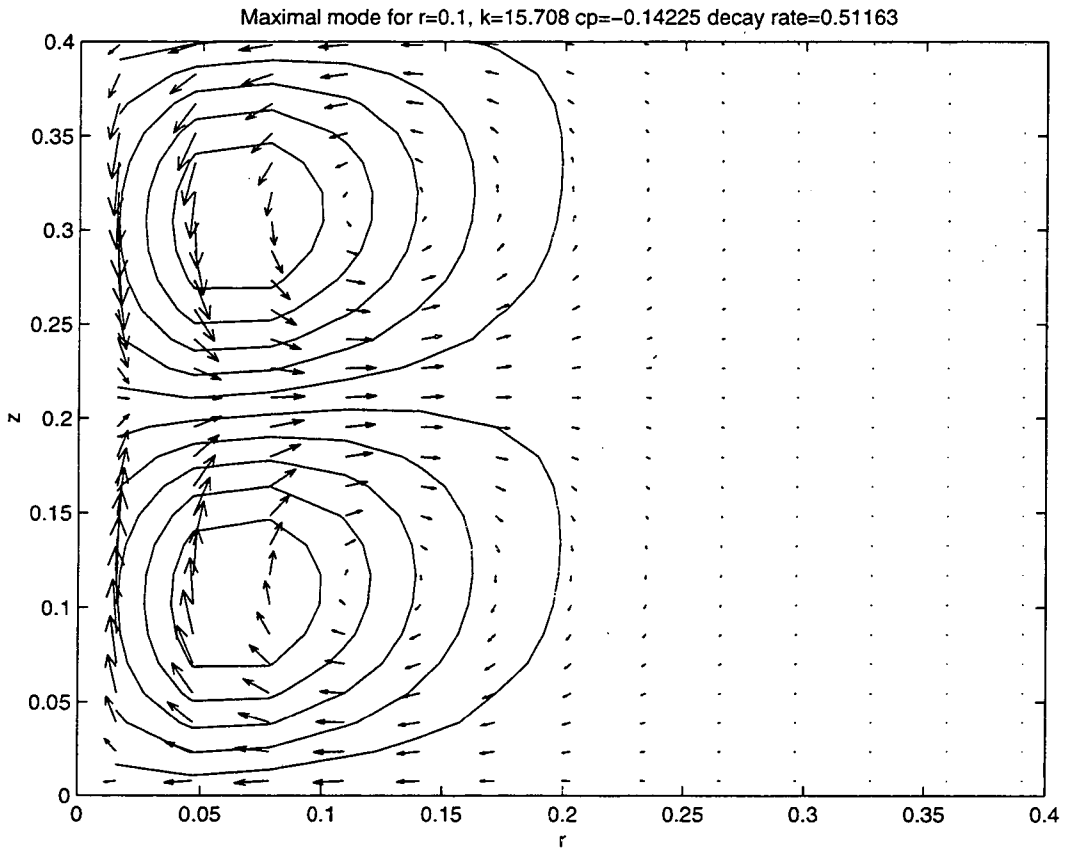

Figure 19 Modal structure with vertical wavelentgh 0.4 and maximum radial velocities at r=0.1 found from eigenanalysis of the vortex core in the high-swirl case.

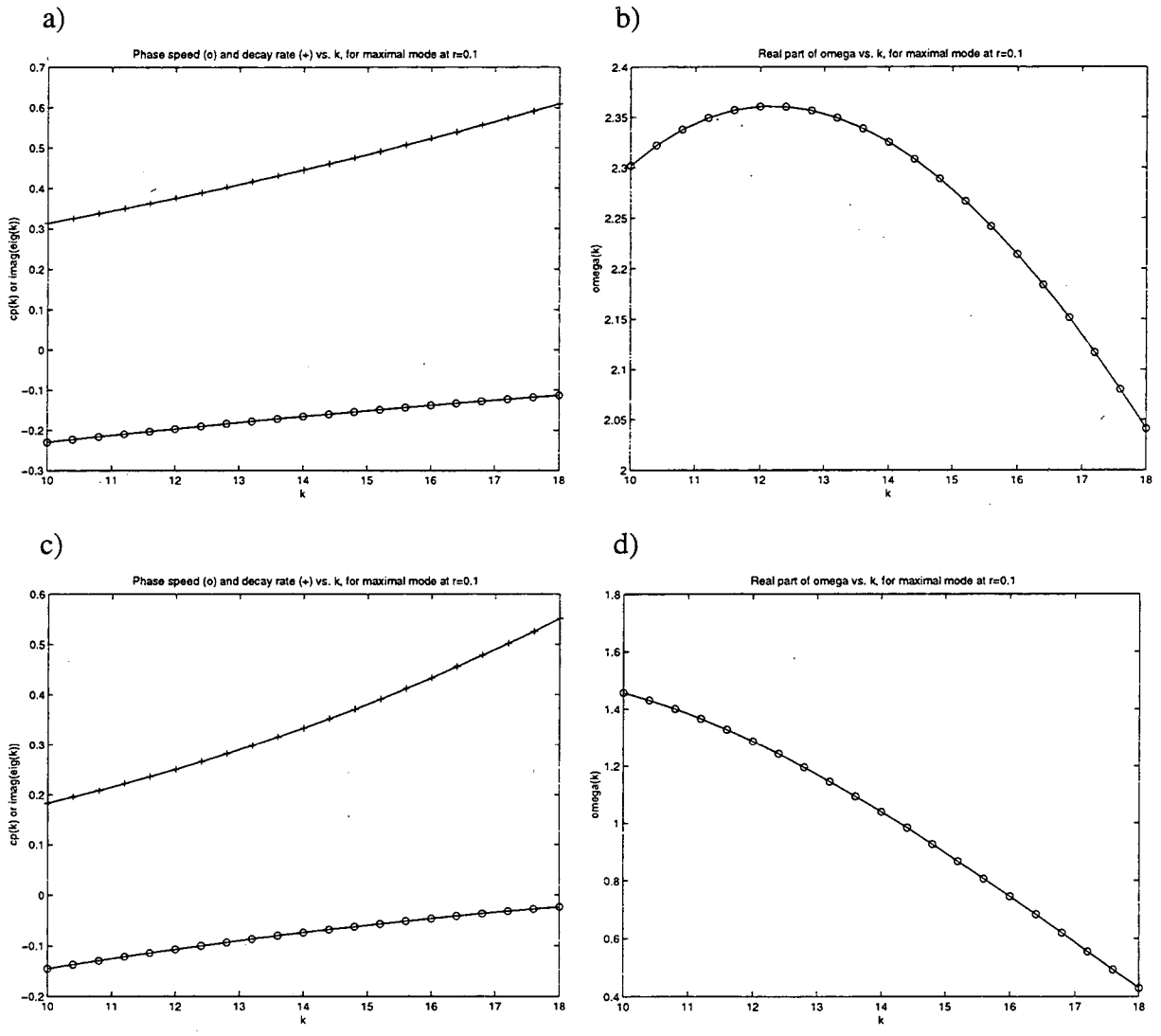

Figure 20 Plots of phase speed, decay rate, and the real parts of ω versus vertical wave-number k for the modes with maximum amplitude at r=0.1: a) phase speed and decay rate, high swirl case; b) ω, high-swirl case; c) phase speed and decay rate, low-swirl case; d) ω, low-swirl case.

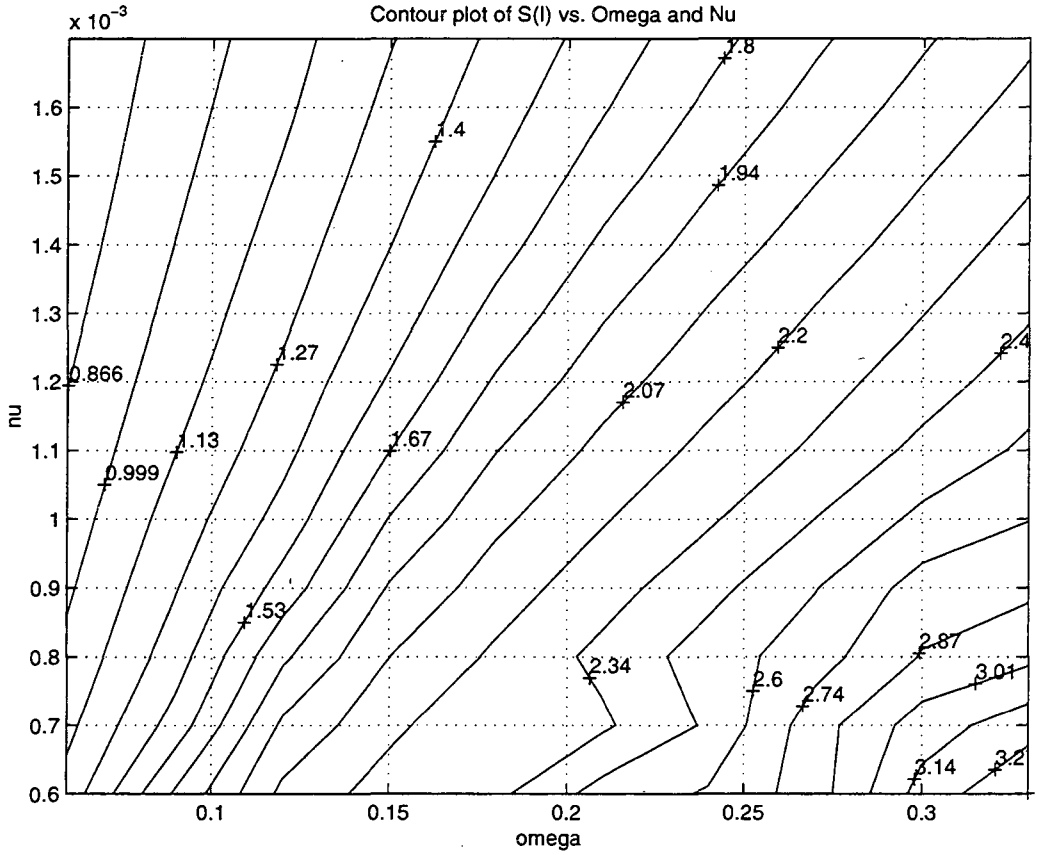

Figure 21 Contour plot of the mean value of the internal swirl ratio as a function of the domain rotation rate Ω and the eddy viscosity ν.

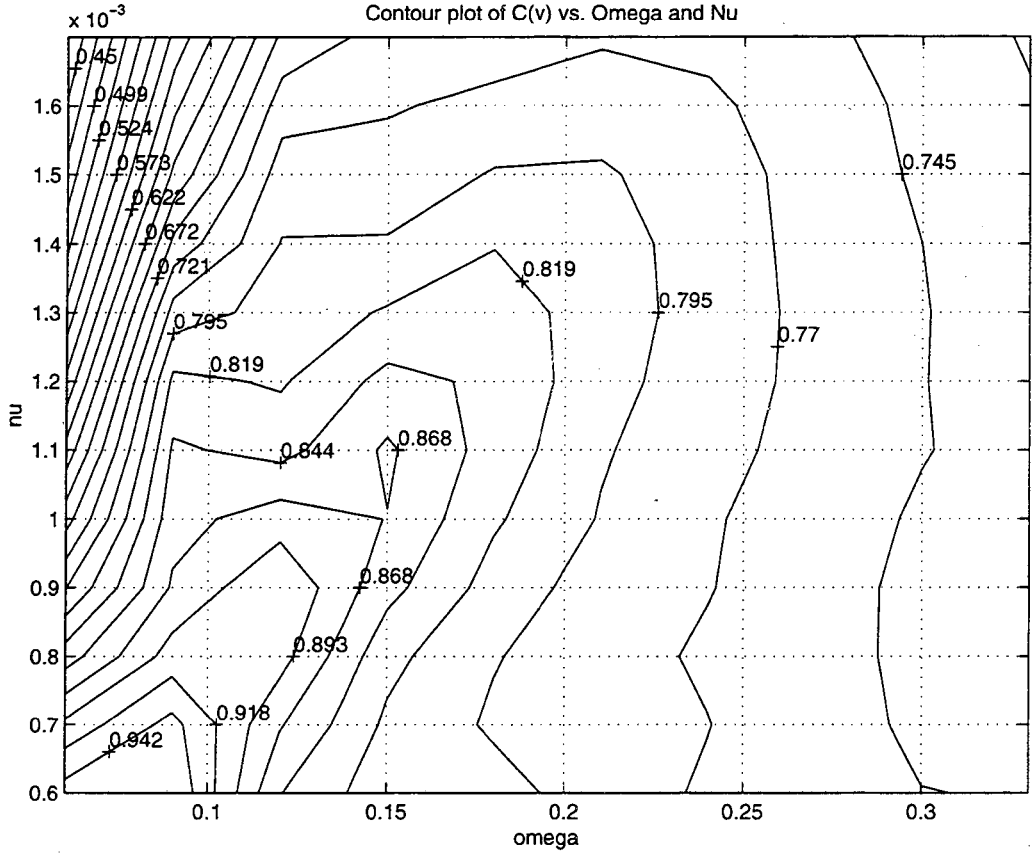

Figure 22 Contour plot of the mean value of the velocity coefficient C_v as a function of the domain rotation rate Ω and the eddy viscosity ν.

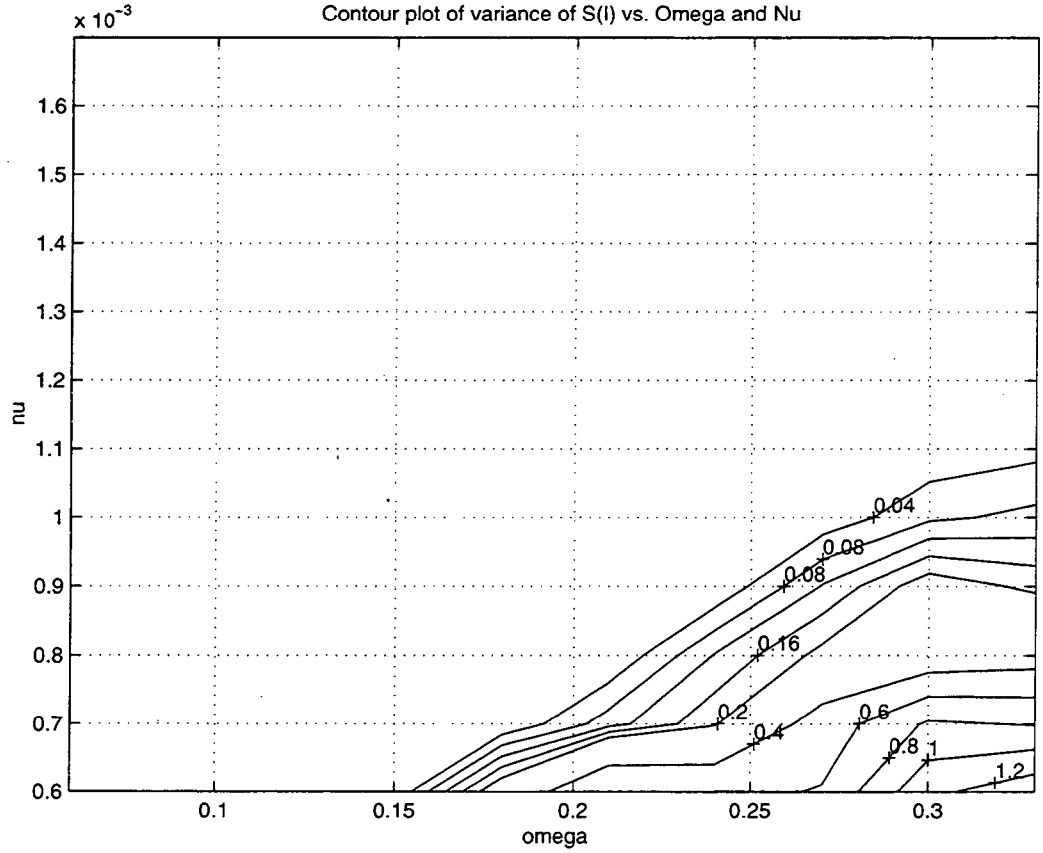

Figure 23 Contour plot of the variance of the internal swirl ratio S_I as a function of the domain rotation rate Ω and the eddy viscosity ν. Due to the wide range in values for the variance, the contour levels have been chosen arbitratily to have the following values : 0.04, 0.08...0.16; 0.2, 0.4....1.2.

Ernest Orlando Lawrence Berkeley National Laboratory
One Cyclotron Road | Berkeley, California 94720

Prepared for the U.S. Department of Energy under Contract No. DE-AC03-76SF00098